The role of transient receptor potential canonical type 6 (TRPC6) channels in regulating ventral tegmental area dopamine neuron physiology and function

Mollie Bernstein

A dissertation
submitted in partial fulfillment of the
requirements for the degree of

Doctor of Philosophy

University of Washington
2025

Reading Committee:
Larry Zweifel, Chair
Brock Grill
Susan Ferguson

Program Authorized to Offer Degree:
Neuroscience

University of Washington

Abstract

The role of transient receptor potential canonical type 6 (TRPC6) channels in regulating ventral tegmental area dopamine neuron physiology and function

Mollie Bernstein

Chair of the Supervisory Committee:
Larry Zweifel
Department of Psychiatry and Behavioral Sciences

Ventral tegmental area (VTA) dopamine (DA) neurons integrate neurotransmitter and neuropeptide signals to encode reward-related information. Extensive work from our laboratory and others has shown how specific subpopulations of VTA-DA neurons, defined by the expression of neuropeptide G-protein coupled receptors (GPCRs), regulate motivated behavior. These neuropeptide GPCRs activate signaling pathways that lead to increases in intracellular calcium ions, affecting cellular function and ultimately behavior. However, the mechanisms of these increases in intracellular calcium ions remain largely unexplored.

Transient receptor potential canonical (TRPC) channels are a class of calcium-permeable ion channels, and our laboratory has identified TRPC type 6 (TRPC6) channels as the most

abundantly expressed TRPC channel in VTA-DA neurons. Given strong evidence linking TRPC channel activation with neuropeptide receptor signaling, neuropeptidergic modulation of calcium signaling dynamics in VTA-DA neurons, and the widely established role of DA neurons encoding reward-related information, we hypothesized that TRPC6 channels are critical regulators of neuropeptidergic signaling pathways in VTA-DA neurons.

To explore this, we disrupted TRPC6 channel function in DA neurons of the adult mouse VTA and performed *ex vivo* calcium imaging, whole-cell patch-clamp electrophysiology and *in vivo* fiber photometry during consummatory tasks. We demonstrate a novel mechanism by which TRPC6 channels regulate distinct aspects of neuropeptide receptor-activated calcium signals in VTA-DA neurons but make little contribution to the calcium dynamics associated with metabotropic neurotransmitter receptor signaling. Additionally, we show that TRPC6 channels regulate scalable reward valuation and consummatory behavior in a homeostatic state-dependent manner. Future studies will explore the single-cell calcium dynamics of TRPC6 channel-mediated signaling *in vivo,* the signaling complexes involved in the control of TRPC6 channel activation by neuropeptide receptors, and the role of other neuropeptidergic inputs to VTA-DA neurons that influence TRPC6 channel recruitment under varying homeostatic states.

TABLE OF CONTENTS

FIGURES AND TABLES

ACKNOWLEDGEMENTS

Firstly I would like to thank Larry and the entire Zweifel/Soden labs for their support and feedback. I remember the first lab meeting that I gave five years ago and how nervous I was to present in front of all of you whom I had only met a few months prior. Now, I am much calmer when presenting because you have all become friends and colleagues rather than scary scientists. I thank everyone for their feedback, suggestions and practice questions that have made me a better scientist. I would especially like to thank former Zweifel lab members: Meagan for being my first mentor in the lab and introducing me to all things CRISPR and cloning; Barb for the insightful suggestions at every one of my lab meetings; Chris for sharing the scripts that was the impetus for my journey into coding. Larry, thank you for the mentorship, guidance, and feedback on all of my numerous written drafts, presentations, posters, and figures. I am sure it gets repetitive reading variations of the same documents over and over again, but I learn something new every time I send you a document for comments.

I would like to thank my committee members (Brock Grill, Susan Ferguson, Jane Sullivan, Marti Bosma, Steve Perlmutter) for their expertise, suggestions for new/alternative experiments, and support when I presented the challenges I had to overcome. Your insight prepared me for questions I encountered while presenting at conferences and for questions I will no doubt receive in the future.

Thank you to the entire Neuroscience Graduate Program and 2020 cohort. We started graduate school at a very uncertain and isolating time but have pushed through these additional challenges and are all defending soon. I am proud of us!

Thank you to all the mentors I had prior to graduate school who *are the reason* I entered graduate school. First, to Matt Carter for his ability to teach neuroscience in such an exciting way that I had to learn more and for suggesting that I consider rotating in Larry's lab. Second, to Allan Basbaum for inspiring me to choose graduate school over medical school ("when you're in graduate school and you discover something new, you're *the only* person in the whole world know knows it"). I would also like to thank Jarret Weinrich and Cindy Liu in the Basbaum Lab for the graduate school application help and much more.

Special thank you to my Seattle bike and swim friends (Chris Z., Chris K., Katie, Stephen, Jon, Rachel, Nikki, Anna) who I was able to ride and swim with during the pandemic. Without you graduate school would have been very isolating.

Finally, thank you to my entire family (that has doubled while in graduate school – Simon, Vivian, Joey, Alda) for their unconditional love and support. And last but not least, thank you to my husband, Daniel! I couldn't have done it (the degree and the analysis ☺) without you.

DEDICATION

To my parents. Thank you for everything.

CHAPTER 1: INTRODUCTION

Midbrain dopamine (DA)-producing neurons of the ventral tegmental area (VTA) play a critical role in regulating reward-seeking behavior (Wise, 2004). In addition to producing DA, VTA-DA neurons are also enriched in neuropeptides and neuropeptide receptors (Heymann et al., 2020). Neuropeptide receptors are G-protein coupled receptors (GPCRs) and neuropeptidergic signaling potently modulates VTA-DA neuron activity to rewarding stimuli (Soden et al., 2023; Elum et al., 2024). However, the specific mechanisms that control intracellular calcium signaling pathways downstream of neuropeptide receptor activation in VTA-DA neurons remain unknown.

Transient receptor potential canonical (TRPC) channels are a class of calcium-permeable ion channels activated by downstream signaling molecules generated by GPCR activation (Zhang et al., 2023; Wang et al., 2020) but have not been thoroughly explored in the context of modulating VTA-DA neuron activity. Our laboratory has identified TRPC type 6 (TRPC6) channels as the most abundantly expressed TRPC channel in VTA-DA neurons. Given strong evidence linking TRPC channel activation with neuropeptide receptor signaling (Stuhrman et al., 2015; Kelly et al., 2018; Qiu et al., 2021), neuropeptidergic modulation of calcium signaling dynamics in VTA-DA neurons (Soden et al., 2023), and the widely established role of DA neurons in encoding reward-related information (Wise et al., 2004), we hypothesized that TRPC6 channels are critical regulators of VTA-DA neuron calcium signaling dynamics and reward learning.

1.1 Neuropeptidergic signaling in VTA-DA neurons

VTA-DA neurons, which comprise approximately two thirds of VTA cells, regulate many aspects of motivated behavior: scaling responses to rewards of different sizes and value, signaling reward prediction errors when rewards are unexpectedly omitted, and regulating reward-seeking behavior (Wise et al., 2004). VTA-DA neurons can also be genetically defined by the neuropeptides and neuropeptide receptors that they express, in addition to dopamine (Heymann et al., 2020; Simon et al., 2024). Two large populations of interest for our laboratory are the neurotensin receptor 1 (*Ntsr1*)-expressing population and the tachykinin receptor 3 (*Tacr3*)-expressing population. We have shown that neuropeptidergic inputs to these subpopulations differentially modulate VTA-DA neuron activity to rewards through the coordination of opposing neuropeptide and neurotransmitter signals (Soden et al., 2023). Specifically, the inputs of inhibitory neurotransmitter GABA and stimulatory neuropeptide (e.g. neurotensin) onto VTA-DA neurons leads to neuropeptide receptor activation, resulting in an increase in intracellular calcium ions (Ca^{2+}) (Soden et al., 2023). While neuropeptide receptor activation in the context of reward learning leads to distinct calcium dynamics and dysregulation of calcium signaling in DA neurons has been shown to severely disrupt cell excitability and reward learning (Zweifel et al., 2009), the specific ion channels downstream of neuropeptide receptor activation that regulate intracellular Ca^{2+} flux in DA neurons are still under investigation.

1.2 A note on calcium signaling

Calcium ions are key second messenger molecules involved in numerous signaling cascades, including synaptic plasticity, neuronal excitability, synaptic transmission and transcription (Clapham, 2007). Ca^{2+} flux is tightly controlled by multiple types of ion channels embedded within the plasma membrane and endoplasmic reticulum (Clapham, 2007). Voltage-gated calcium channels (VGCC) are activated by changes in membrane potential and are the primary pathway for extracellular Ca^{2+} entry into the cytoplasm (Catterall, 2011; Simms & Zamponi, 2014). VGCCs are well-characterized in DA neurons (Liu et al., 2014; Tracy et al., 2018), but do not fully explain the intricate dynamics of intracellular Ca^{2+} flux.

1.3 GPCR ($G_{\alpha q/11}$) signaling pathways

Neuropeptide receptors are a class of G-protein coupled receptors (GPCRs) that, once activated, initiate multiple signaling cascades resulting in increases in intracellular Ca^{2+} (Clapham, 2007). Ntsr1 and Tacr3 signal through stimulatory $G\alpha_{q/11}$ G proteins (Torruella-Suárez & McElligott, 2020; Zhang et al., 2020). Upon binding of a ligand, phospholipase C (PLC) is activated, which cleaves PIP_2 into IP_3 and diacylglycerol (DAG). DAG in turn activates protein kinase C (PKC), which then phosphorylates other proteins, leading to multiple cellular responses. The canonical view of the downstream effects of Ca^{2+} influx initiated by neuropeptide receptor activation involves the PKC signaling cascade. However, recent evidence suggests that transient potential receptor canonical (TRPC) channel-mediated signaling is a large driver of Ca^{2+} influx induced by neuropeptide receptor activation (Stuhrman et al., 2015; Kelly et al., 2018; Qiu et al., 2021).

1.4 A brief introduction to TRPC channels

TRPC channels are a class of calcium-permeable ion channels embedded in the plasma membrane (Wang et al., 2020). They are a part of the TRP superfamily, first discovered in *Drosophila* and best known for the TRPV heat sensitive subtype. There are seven mammalian types (1-7) of the TRPC family, which are further subdivided into three subtypes (TRPC1/4/5, TRPC2, and TRPC3/6/7) based on their sequence homology and functional similarities (Wang et al., 2020; Zhang et al., 2023), and the mode of activation differs for each subtype. For example, TRPC5 channels operate as both receptor-operated and store-operated channels. In a receptor-operated role, TRPC5 channels are activated by $G_{q/11}$ stimulation, leading to PKC phosphorylation and direct binding of DAG to the channel, which allows Ca^{2+} to flow into the cell (Ningoo et al., 2021; Kelly & Wagner, 2024). In a store-operated role, TRPC5 channels couple to the STIM/Orai complex at the endoplasmic reticulum (ER)-plasma membrane (PM) junction upon IP_3R-mediated depletion of Ca^{2+} stores from the ER. Here, TRPC5 channels allow Ca^{2+} to flow from the extracellular space directly into the ER to refill ER Ca^{2+} stores (Qiu et al., 2021). In contrast, TRPC6 channels only have one mode of activation, which is direct binding of DAG to the channel (Wang et al., 2020).

1.5 TRPC channels as downstream effectors of GPCR signaling pathways

TRPC channels are downstream effectors of GPCR signaling. For example, TRPC1/4/5 channels are linked to metabotropic glutamate receptor (a type of GPCR) signaling in hippocampal CA1 neurons (El-Hassar et al., 2011). In this context, TRPC1/4/5 channels regulate a second wave of increase in Ca^{2+} that is independent of the first wave of Ca^{2+} from VGCCs (El-Hassar et al., 2011).

Recent work has focused on the role of TRPC5 channels in regulating neuronal excitability and calcium signaling dynamics in *Kisspeptin* (*Kiss1*)-expressing neurons in the arcuate nucleus (ARH). Qiu et al. (2016) demonstrated that both *Trpc5* and *Tacr3* mRNA are highly enriched in ARH-*Kiss1* neurons and that activation of Tacr3 in ARH-*Kiss1* neurons leads to the opening of TRPC5 channels, causing a robust depolarization. This signaling pathway, along with co-release of dynorphin, coordinates the synchronous firing of ARH-*Kiss1* neurons (Kelly & Wagner, 2024). To investigate the role of TRPC5 channels as store-operated channels through coupling to the STIM/Orai complex (that senses depletion of intracellular Ca^{2+} and refills ER intracellular Ca^{2+} stores), Qiu et al. (2021) selectively deleted *Stim1* in ARH-*Kiss1* neurons. Deletion of *Stim1* in ARH-*Kiss1* neurons significantly increased the amplitude and duration of the slow depolarization, as well as augmented senktide-induced synchronous calcium oscillations (Qiu et al., 2021). Together, these results demonstrate that TRPC5 channels play a critical role in regulating excitability and synchronous activity of ARH-*Kiss1* neurons through their dual roles as receptor-operated channels (via Tacr3 activation) and store-operated channels (via STIM/Orai activation) (Wagner & Kelly, 2024).

1.6 TRPC channels in VTA-DA neurons: what's known?

We analyzed our laboratory's previously published dataset (Chung et al., 2017) and identified *Trpc6* mRNA as the most abundantly expressed TRPC channel mRNA in VTA-DA neurons (Fig. iA). This finding is consistent with *in situ* data from the Allen Institute brain atlas showing an enrichment of *Trpc6* mRNA in the VTA (Lein et al., 2007). Given the functional significance of neuropeptidergic signaling in the VTA and high enrichment of TRPC6 channels in VTA-DA neurons, we hypothesized that TRPC6 channels are downstream of neuropeptide receptors in VTA-DA neurons (Fig. iB).

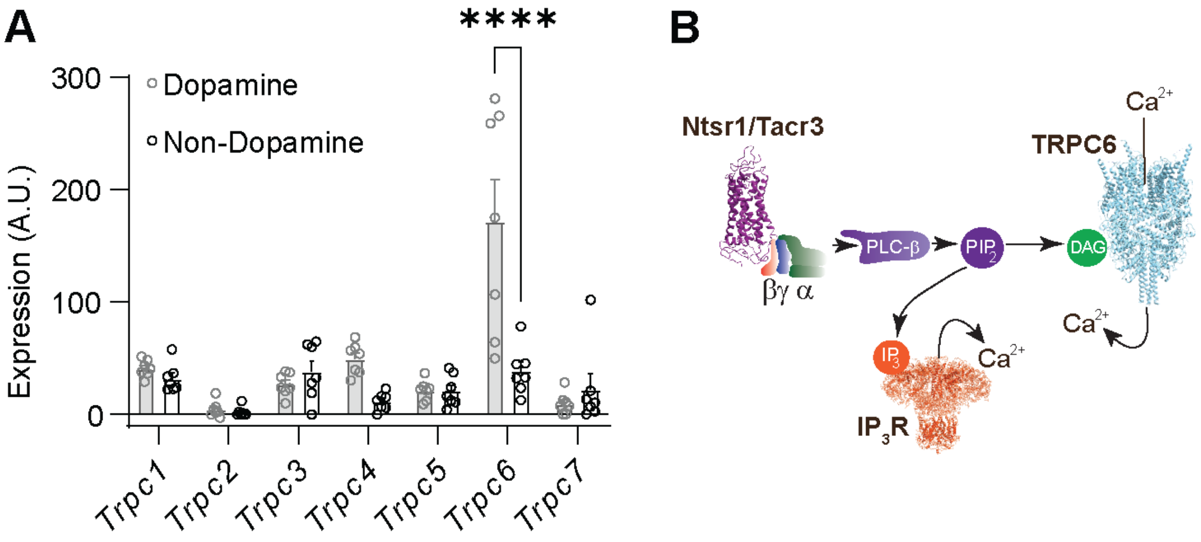

Figure i. TRPC6 channels in the VTA. (A) mRNA expression of TRPC channel encoding genes in the VTA of adult mice (Two-way RM ANOVA followed by Bonferroni post hoc comparison. N=7 mice for both groups, ****$p<0.0001$). (B) Hypothesized signaling pathway: GPCR activation initiates a signaling cascade resulting in an increase in intracellular Ca^{2+} through TRPC6 channels and IP$_3$Rs.

Indirect evidence supports the functional role of TRPC channels in VTA-DA neurons. Using a nonspecific TRPC channel blocker, Stuhrman et al. (2015) demonstrated that neurotensin-activated inward current is partially mediated by general TRPC channel activation in VTA-DA neurons. Another study found that *Trpc4* was most abundantly expressed in VTA neurons in rats (Kilpec et al., 2016). Using a brain wide knock out of *Trpc4,* the authors found reduced cocaine self-administration and reduced spontaneous VTA-DA neuron activity, without deficits in learning for natural rewards (Kilpec et al., 2016). More recently, Wang et al. (2024) confirmed high expression of *Trpc6* in VTA-DA neurons in mice using single-cell RNA-sequencing. Using a scrambled short hairpin RNA knockdown approach, they found that downregulation of TRPC6 channels induces a profound decrease in spontaneous firing of VTA-DA neurons (Wang et al., 2024). Despite all of this evidence, the role of TRPC6 channels in regulating neuropeptidergic signaling, calcium dynamics, and reward-related behavior in VTA-DA neurons remains unexplored.

1.7 TRPC6 channels more broadly

TRPC6 channels have been investigated in the context of other disorders and model systems; these findings highlight important considerations that have implications for our hypothesis. Two studies report opposing effects to Wang et al. (2024)'s findings of decreased mobility and cell excitability and after TRPC6 channel knockdown. Mutations in *trpγ*, the homologue of TRPC6 autism candidate gene, causes autism-like behavioral deficits in *Drosophila,* including hyperactivity (Palacios-Muñoz et al., 2022). Another study found that TRPC6 knockout induces hyperexcitability in cortical neurons derived from human pluripotent stem cells (Shin et al., 2023).

TRPC6 channels have also been studied in the context of depression (Hamdaoui et al., 2022; Wang et al., 2024), memory (Zernov & Popugaeva, 2023), and locomotion (Yeon et al., 2018). Brain-wide TRPC6 channel knockout mice exhibit anxious and depressive behavior compared to wild-type mice (Hamdaoui et al., 2022; Wang et al., 2024), as well as reduced hippocampal excitability in CA1 neurons (Hamdaoui et al., 2022). Interestingly, hyperforin, the active ingredient in St. John's wort that has mild antidepressant action, has also been shown to activate TRPC6 channels (Hamdaoui et al., 2022). While beyond the scope of this work, these findings suggest a role for TRPC6 channels as a potential therapeutic candidate for treatment of autism, anxiety, and depressive disorders.

1.8 Hypothesis and approach

In sum, the literature suggests an important role for TRPC6 channels in VTA-DA neuron physiology and function, but also raises questions due to conflicting evidence, specifically in terms of TRPC6 channels' role in neuronal excitability. Additionally, these studies did not examine the specific and/or selective coupling of different types of GPCRs and TRPC6 channels. This is surprising given that TRPC6 channels are known to be activated by DAG, a direct product of GPCR activation. Therefore, my dissertation aims to evaluate whether TRPC6 channels affect neuropeptide receptor-mediated modulation of neuronal excitability, calcium signaling dynamics, and reward-related behavior in VTA-DA neurons.

CHAPTER 2: A NEUROPEPTIDE-SPECIFIC SIGNALING PATHWAY FOR STATE-DEPENDENT REGULATION OF THE MESOLIMBIC DOPAMINE SYSTEM

This chapter is available as a preprint on bioRxiv and will be submitted for publication.

Mollie X. Bernstein, Omar Koita, Marta Trzeciak, Andrew Fan, Daniel T. McAuley, Seung-Woo Jin and Larry S. Zweifel

Dopamine (DA)-producing neurons of the ventral tegmental area (VTA) regulate consummatory behavior in a state-dependent manner (e.g. when hungry or thirsty). The mechanisms by which and extent to which DA neurons are regulated by these interoceptive signals are poorly understood. Here, we identify transient receptor potential canonical type 6 (TRPC6) channels as selective mediators of neuropeptide receptor-induced calcium signaling in VTA-DA neurons. These channels regulate DA neuron activity and consummatory behavior in a state-dependent manner. We find that TRPC6 channels regulate distinct aspects of neuropeptide-induced calcium signals in DA neurons but make little contribution to calcium dynamics associated with metabotropic neurotransmitter receptor signaling. We further show that TRPC6 channels regulate scalable reward valuation and consummatory behavior in hungry but not thirsty mice. These findings demonstrate that neuropeptide- and neurotransmitter-activated G-protein coupled receptors (GPCRs) regulate cellular calcium dynamics through distinct mechanisms, and that TRPC6 channels are important determinants of how animals respond to different homeostatic demands.

2.1 Introduction

Midbrain dopamine (DA)-producing neurons of the ventral tegmental area (VTA) play a critical role in scaling responses to rewards and regulating reward-seeking behavior (Wise, 2004), as well as in homeostatically driven fluid and food consumption (Mietlicki-Baase et al., 2021; Palmiter, 2007). Numerous neuropeptides that regulate energy balance and homeostatic fluid and food consumption modulate the activity of VTA DA neurons (Khan et al., 2024; Naef et al., 2015; Palmiter, 2007), and several of these have been shown to increase DA neuron activity and dopamine release (Cone et al., 2014; Nalivaiko et al., 1997; Seutin et al., 1989). These stimulatory neuropeptides typically signal through GPCRs that are coupled to $G_{q/11}$-mediated signaling cascades to increase intracellular calcium, but the mechanisms through which they modulate VTA-DA neurons are largely unknown.

The two most abundantly enriched stimulatory neuropeptide receptors in VTA-DA neurons are the neurotensin receptor (Ntsr1) and the neurokinin B (also known as tachykinin 2) receptor (Tacr3) (Chung et al., 2017). Ntsr1 and Tacr3 are stimulatory $G\alpha_{q/11}$-protein coupled receptors (GPCRs) and upon ligand binding, phospholipase C (PLC) is activated, which cleaves PIP_2 into IP_3 and diacylglycerol (DAG). Generation of IP_3 activates IP_3 receptors on the endoplasmic reticulum to induce intracellular calcium release (Clapham, 1995). DAG, in turn, activates protein kinase C (PKC), which then phosphorylates other proteins, leading to multiple cellular responses, including the phosphorylation of ion channels to regulate neuronal excitability (Kaczmarek, 1987). PIP_2 is a critical co-factor for the Kv7 family of voltage-gated potassium channels; thus, PIP_2 hydrolysis also results in membrane depolarization (Suh & Hille, 2002) which can, in turn, activate voltage-gated calcium channels (VGCCs) (Mathes and Thompson, 1994).

An additional mechanism for the regulation of extracellular calcium influx and the modulation of neuronal excitability through neuropeptide signaling is the transient receptor potential canonical (TRPC) channels (Kelly et al., 2018; Qiu et al., 2021; Stuhrman and Roseberry, 2015). TRPC channels are a class of calcium-permeable ion channels (Wang et al., 2020), subdivided into 3 subtypes (TRPC1/4/5, TRPC2, and TRPC3/6/7) based on their sequence homology and functional similarities (Wang et al., 2020; Zhang et al., 2023). In *Kisspeptin* (*Kiss1*)-expressing neurons in the arcuate nucleus (ARH), activation of the Tac2/NkB receptor Tacr3 results in a TRPC5-dependent membrane depolarization (Qiu et al., 2016). Tac2/NkB along with the co-release of dynorphin, coordinates the synchronous firing of ARH-*Kiss1* neurons (Kelly and Wagner, 2024).

Given the high expression of *Tacr3* in VTA-DA neurons, we hypothesized that Tacr3-dependent activation of a TRPC channel is an important regulatory pathway for neuropeptide modulation of VTA-DA neurons. Of the TRPC channels, the receptor operated channel TRPC6 is highly enriched in DA neurons (Chung et al., 2017) and is the most abundantly expressed TRPC channel in these cells (Wang et al., 2024). Using a cell-type-specific CRISPR/Cas9 mutagenesis approach, we demonstrate that TRPC6 channels are selectively involved in rapid neuropeptide receptor-induced calcium influx, but not neurotransmitter receptor-induced calcium increases. We further find that TRPC6 channels regulate neuropeptide-induced synchronous calcium increases and calcium oscillations in VTA dopamine neurons. During liquid sucrose consumption in thirsty or hungry mice, we find that genetic inactivation of *Trpc6* impairs scalar consummatory responses to increasing sucrose concentrations and scalar increases in calcium signals in VTA-DA neurons in hungry but not thirsty mice. These findings demonstrate that TRPC6 channels act downstream of stimulatory neuropeptide receptor signaling and modulate consummatory responses in a state-dependent manner.

2.2 Results

2.2.1 CRISPR/SaCas9 mutagenesis of *Trpc6* in VTA-DA neurons.

To confirm that *Trpc6* is the predominant TRPC channel expressed in DA neurons, we analyzed our previously published dataset of actively translated mRNA from VTA-DA neurons (Chung et al., 2017). Among the seven TRPC channel genes, *Trpc6* is the most abundantly expressed and is highly enriched in VTA-DA neurons relative to other VTA cell types (Fig. 1A), consistent with previous reports (Wang et al., 2024). RNAscope *in situ* hybridization analysis further demonstrated that *Trpc6* expression is localized to a large proportion of *Th*-positive cells (a marker for DA cells) and is relatively restricted to expression in VTA-DA neurons (Fig. 1B).

To investigate the function of TRPC6 channels in VTA-DA neurons, we selectively mutated the *Trpc6* gene using viral-mediated cell-type-specific CRISPR/Cas9 mutagenesis (Hunker et al., 2020). We designed two separate sgRNAs targeting different exons in the *Trpc6* gene, to generate two viral constructs: AAV1-CMV-FLEX-SaCas9-U6-sg*Trpc6*(1) and AAV1-CMV-FLEX-SaCas9-U6-sg*Trpc6*(2) (Fig. 1C). Deep sequencing of PCR amplicons containing the sgRNA targeted regions revealed a high degree of insertion and deletion mutations (indels) (Fig. 1D-E).

To confirm loss of TRPC6 channel function, we co-injected DAT-Cre mice with either AAV1-FLEX-sg*Rosa26* or a mixture of AAV1-FLEX-sg*Trpc6*(1) and AAV1-FLEX-sg*Trpc6*(2), along with the genetically encoded calcium indicator GCaMP8f into the VTA. We assessed calcium influx in VTA-DA neurons in acute brain slices following a brief (50 ms) focal application (puff) (Forman et al., 2017) of the TRPC6 channel agonist GSK1702934A.

A 50 ms puff resulted in large increases in calcium fluorescence in sg*Rosa26* control cells at a high (1 µM GSK1702934A) (Fig. 1F-G) and intermediate (0.3 µM GSK1702934A) concentration (Fig. 1I-J). These responses were significantly attenuated in sg*Trpc6* cells for both concentrations of GSK1702934A (Fig. 1F-G, I-J). VTA-DA neurons in the sg*Trpc6* group also displayed a significant reduction in the proportion of responsive and nonresponsive cells for both 1 µM GSK1702934A (Fig. 1H) and 0.3 µM GSK1702934A (Fig. 1K). Together, these data confirm the high functional efficiency of *Trpc6* mutagenesis in VTA-DA neurons.

2.2.2 TRPC6 channels are selectively coupled to neuropeptide receptor activation.

Based on the evidence linking TRPC5 channels to Tacr3 signaling (Kelly and Wagner, 2024) and the high expression of *Tacr3* in VTA-DA neurons (Chen et al., 1998; Chung et al., 2017), we first performed *ex vivo* calcium imaging of VTA-DA neurons using the Tacr3 agonist senktide. As above, DAT-Cre mice were bilaterally injected with either AAV1-FLEX-sg*Rosa26* or a combination of AAV1-FLEX-sg*Trpc6*(1) and AAV1-FLEX-sg*Trpc6*(2) along with AAV1-FLEX-GCaMP8f into the VTA. We observed a large increase in calcium fluorescence in response to a puff of 0.5 µM senktide, which was significantly reduced in the sg*Trpc6* group quantified as both AUC and peak amplitude (Fig. 2A). There was no significant difference in the proportion of responsive versus nonresponsive cells (Fig. 2A).

In ARH-*Kiss1* neurons, bath application of senktide results in a TRPC5-dependent, STIM/ORAI-independent, augmentation of the synchronous calcium rise in these cells (Qiu et al., 2021). To assess whether TRPC6 mediates a similar function in VTA-DA neurons, we bath applied senktide (500 nM) to acute brain slices from DAT-Cre mice injected with either AAV1-FLEX-sg*Rosa26* or AAV1-FLEX-sg*Trpc6*(1) and AAV1-FLEX-sg*Trpc6*(2) along with AAV1-FLEX-GCaMP8f into the VTA. Both groups exhibited large increases in calcium fluorescence following senktide application (Fig. 2B). Consistent with TRPC6-dependent rapid calcium increases associated with brief, focal senktide application (Fig. 1A), the initial rate of rise (1/s) was significantly slower in sg*Trpc6* cells compared to control sg*Rosa26* cells (Fig. 2B). To determine whether TRPC6 channels facilitate the synchronous rise in calcium following Tacr3 activation, we assessed the variance (percent coefficient of variation around the mean rise at $T_{1/2}$) of calcium increases within a slice. The variance in sg*Trpc6* cells was significantly increased compared to sg*Rosa26* cells (Fig. 2C).

During our analysis, we observed three distinct responses in calcium signals in VTA-DA neurons to senktide application. The largest number of cells (Type I) displayed a sustained increase in calcium, followed by cells with a sustained increase coupled with oscillatory calcium signals (Type II), and a rarer group of cells (~1%) which showed intrinsic calcium oscillations enhanced by senktide (Type III) (Fig. 2D). Mutagenesis of *Trpc6* resulted in a significant reduction in the number of oscillating cells induced by senktide compared to controls (Fig. 2D). Of the cells in which senktide-induced oscillations were observed, the frequency of oscillations was significantly reduced in sg*Trpc6* cells compared to sg*Rosa26* cells (Fig. 2E); however, the amplitude of the oscillation was unaffected (Fig. 2E).

In addition to *Tacr3,* the NTS receptor NTSR1 (*Ntsr1*) is highly expressed in VTA-DA neurons and facilitates a robust increase in intracellular calcium *in vivo* (Soden et al., 2023). Application of a non-selective TRPC channel blocker also attenuates the neurotensin-mediated inward current in VTA-DA neurons (Stuhrman and Roseberry, 2015). To assess whether TRPC6 acts downstream of NTSR1 activation, we focally applied NTS (1 μM) as above (50 ms puff). NTS-evoked calcium was significantly reduced in sg*Trpc6* cells as quantified by AUC and peak amplitude compared to sg*Rosa26* cells (Fig. 2F).

In other cell types, TRPC6 channels are downstream of other types of GPCRs that cause production of DAG, such as metabotropic glutamate receptors (mGluR) (Wang et al., 2019) and muscarinic acetylcholine receptors (mAChR) (Zhang et al., 2006). To determine whether TRPC6 channels are general downstream effectors of $G_{q/11}$-coupled receptors, we focally applied the mGluR agonist (S)-3,5-Dihydroxyphenylglycine (DHPG) and the mAChR agonist carbachol to VTA-DA neurons. Both DHPG (30 μM) and carbachol (10 μM) induced rapid and robust increases in intracellular calcium (Fig. 2G-H). *Trpc6* mutagenesis did not affect DHPG-evoked calcium signals in VTA-DA neurons (Fig. 2G) and had only a modest but significant effect on the peak carbachol-evoked calcium signal, without affecting the overall calcium signal (Fig. 2H). These results suggest that TRPC6 channels act predominantly downstream of neuropeptide receptor activation (Fig. 2I).

2.2.3 *Trpc6* mutagenesis does not alter spontaneous or evoked action potential firing in VTA-DA neurons.

Previous findings have shown that *Trpc6* knockdown in VTA-DA neurons leads to reduced neuronal intrinsic excitability and resting membrane potential (Wang et al., 2024). However, others have shown that mutagenesis of *TRPC6* in human induced pluripotent stem cell-derived pyramidal neurons causes an increase in neuronal excitability (Shin et al., 2023). To determine whether CRISPR/SaCas9 mutagenesis of *Trpc6* in adult VTA-DA neurons alters neuronal excitability in the absence of neuromodulators, we performed whole-cell patch-clamp recordings in acute brain slices from DAT-Cre mice injected with either AAV1-FLEX-sg*Rosa26* or AAV1-FLEX-sg*Trpc6*(1) and AAV1-FLEX-sg*Trpc6*(2) along with AAV1-FLEX-GcaMP8f (Fig. 3A). We did not observe any significant differences in the proportion of spontaneous versus inactive cells, firing rate, or CV-ISI of spontaneously active cells (Fig. 3B-D). Additionally, we did not observe any differences in resting membrane potential or evoked excitability, as measured by a ramp protocol and current injection (Fig. 3E-H). These results indicate that *Trpc6* loss of function in VTA-DA neurons does not result in an overt change in the intrinsic electrophysiological properties of these cells in the absence of targeted neuropeptide stimulation.

2.2.4 TRPC6 channels regulate consummatory behavior and DA neuron activity in a homeostatic state-dependent manner.

The neuropeptides NTS, Tac2, ghrelin, and angiotensin II are associated with energy balance and fluid/food consumption, and they signal through $G_{q/11}$-coupled receptors. All of these neuropeptides have been shown to modulate DA neuron activity (Cone et al., 2014; Hsu et al., 2020; Naef et al., 2015; Palmiter, 2007), and NTS has been shown to regulate food reward-associated increase in calcium in VTA-DA neurons *in vivo* in hungry mice (Soden et al., 2023). Our *ex vivo* analysis of calcium signaling dynamics in VTA-DA neurons indicates that TRPC6 channels act directly downstream of stimulatory neuropeptide receptor signaling. Therefore, we asked whether TRPC6 channels influence *in vivo* calcium signaling dynamics of VTA-DA neurons during consummatory behavior in hungry or thirsty mice. To address this, we performed fiber photometry recordings in DAT-Cre mice injected with either AAV1-FLEX-sg*Rosa26* or AAV1-FLEX-sg*Trpc6*(1) and AAV1-FLEX-sg*Trpc6*(2), along with AAV1-FLEX-GCaMP6m into the VTA. An optic fiber was implanted over the injection site (Fig. 4A; Supplementary Fig. 1).

Consummatory licking behavior and photometry recordings were performed in head-restrained mice. Sucrose solutions of varying concentrations were delivered to water- or calorie-restricted mice using a multi-spout system previously described (Gordon-Fennell et al., 2023) (Fig. 4B). Briefly, mice were water restricted to 90% of baseline weight, head restrained and trained to lick five spouts for different concentrations of sucrose (water, 5%, 10%, 20%, and 30% sucrose) across five days. The spout identity was changed daily, and each spout was presented twelve times in a pseudorandom order within a daily session. The trial structure included a three second access period where mice could freely lick for liquid delivery (Fig. 4B). Following water restriction (WR), mice were given *ad libitum* access to water and then calorie restricted to 85% baseline body weight, and the multi-spout experiment was repeated as above.

Under WR, both groups exhibited similar licking behavior for all five solutions (Fig. 4C-D). Linear regression analysis of licks versus spout identity was not significantly different between groups (Fig. 4E). In contrast, under food restriction (FR), sg*Trpc6* mice reached maximal licking at 20% sucrose, whereas *sgRosa26* mice showed maximal licking at 30% sucrose (Fig. 4F-G). Linear regression analysis under FR revealed a significantly stronger relationship between licks and spout identity in sg*Rosa26* control mice relative to sg*Trpc6* mice (Fig. 4H). Both groups showed significantly more licking to water, 5%, and 10% sucrose under WR compared to FR and the effect of spout identity for WR versus FR was significantly greater in both groups (Supplementary Fig. 2C).

Analysis of calcium signals in VTA-DA neurons during the solution access period in the multi-spout assay under WR revealed nearly identical responses in sg*Rosa26* and sg*Trp6* mice (Fig. 5A-B) and the linear relationship between spout identity and calcium signals was similar (Fig. 5C). Under FR, however, sg*Rosa26* mice showed significantly higher calcium signals to 30% sucrose than sg*Trpc6* mice (Fig. 5D-E). While the linear regression analysis of area under the curve (AUC) during the solution access period versus spout identity was not significant between groups (Fig. 5F), within group comparisons revealed higher calcium signals to 30% sucrose compared to 20% sucrose in sg*Rosa26* mice that was not observed in sg*Trpc6* mice (Fig. 5E). These data suggest that *Trpc6* mutagenesis does not impair overall scaling of the VTA-DA neuron signal, but only affects scaling to highly valued rewards (e.g. 20% and 30% sucrose).

Based on the differential effects of *Trpc6* mutagenesis on lick rates and calcium signals between WR and FR, we asked whether these effects were reflected as differences in the calcium signals within groups under these conditions. Comparison of calcium signals in sg*Rosa26* mice revealed significantly reduced responses to water, 5%, and 10% sucrose under WR compared to FR, and significantly greater responses to 30% sucrose under FR (Fig. 5G). Interestingly, sg*Rosa26* mice showed a dip in the calcium signal below baseline during the solution access period under FR, indicative of a reward prediction error (RPE)-like signal (Schultz et al., 1997). In contrast, sg*Trpc6* mice showed only modest but significantly greater calcium signals to 5% sucrose under WR compared to FR, and no difference under other conditions (Fig. 5H). Moreover, these animals did not show the same RPE-like signal under FR that we observed in sg*Rosa26* mice.

VTA-DA neurons have been shown to differentially encode homeostatic states under WR or FR, with cells showing increased activity in the post-consummatory phase following water consumption in thirsty mice (Grove et al., 2022). To address whether TRPC6 channels in VTA-DA neurons influence calcium signals post-consumption, we analyzed the AUC during the post-solution access period. We observed differential responses in sg*Rosa26* mice with higher post-consummatory activity at 10% sucrose with WR greater than FR and at 30% sucrose with FR greater than WR (Supplementary Fig. 3A). In sg*Trpc6* mice, we did observe a significant difference at 20% sucrose with FR greater than WR (Supplementary Fig. 3B). Additionally, similar to consummatory responses and calcium signals during the access period under FR, we observed significant differences between 20% and 30% sucrose in sg*Rosa26* mice during the post-consummatory period that was not significant in sg*Trpc6* mice (Supplementary Fig. 3A-B). We observed no differences between the groups in the linear relationship between post-consummatory calcium signals and spout identity (Supplementary Fig. 3C). Together, these findings demonstrate that TRPC6 channel signaling in DA neurons plays an important role in regulating consummatory responses and the differential encoding of solution content under varying homeostatic states, particularly during the solution access period.

2.3 Discussion

Our findings provide substantial evidence for the specific coupling of TRPC6 channels to neuropeptide receptor signaling pathways in VTA-DA neurons. We demonstrate selective modulation of calcium dynamics following neuropeptide receptor activation of Ntsr1 and Tacr3, whereas activation of other GPCRs (e.g. mGluR, mAChR) that also couple to $G_{q/11}$ signaling do not show the same level of engagement of TRPC6 channels. These GPCR signaling pathways involve PLC-mediated cleavage of PIP_2 into IP_3 and DAG. Despite the high likelihood that the same signaling cascade is utilized by both neuropeptide and metabotropic neurotransmitter receptors, we observed highly selective coupling of TRPC6 channels to neuropeptide receptors. The robust calcium responses to DHPG and carbachol are consistent with previous reports of expression of mGluR5 and m5AchR in VTA-DA neurons (Merrill et al., 2015; Yeomans et al., 2001). This receptor-channel specificity may be attributed to the spatial proximity of TRPC channels relative to their activating GPCRs (Luo et al., 2025). Alternatively, the level of $G_{q/11}$ signaling and regulation could vary with different GPCRs leading to differential effects of TRPC6 channels.

Indeed, scaffolding proteins like A-kinase anchoring proteins (AKAPs) spatially constrain GPCR and ion channel signaling (Wong and Scott, 2004). The proximity between mAChRs and TRPV4 channels in endothelial cells is regulated by AKAP79/150, and the interaction between

TRPV4 and AKAP79/150 is critical for carbachol-induced activation of the channel (Sonkusare et al., 2014). Little is known about interactions between AKAPs and TRPC6 channels; however, AKAP79/150 protein has been detected in VTA-DA neurons (Dacher et al., 2013). Future experiments to determine the signaling complexes involved in the control of TRPC6 activation by neuropeptide receptors will be highly informative.

The functional implications of neuropeptide receptor-TRPC6 channel selective coupling are supported by our *in vivo* data. Our results demonstrate that *Trpc6* mutagenesis directly impacts VTA-DA neuron calcium signaling dynamics associated with consummatory behavior and caloric content. Specifically, we show that TRPC6 channels play an important role in encoding sucrose concentration in a manner that is consistent with reward value encoding and modulating consummatory behavior in response to specific homeostatic demands (hunger versus thirst). Between group comparisons of calcium signals during the multi-sucrose task under food restriction reveal that mutagenesis of *Trpc6* impairs the scaling of VTA-DA neuron calcium signals and subsequent behavioral responses to high-value sucrose rewards.

Within-group comparisons reveal a more complex relationship between TRPC6 channel signaling and scalar encoding of value. Both sg*Rosa26* control and sg*Trpc6* mutants showed increased calcium signals in DA neurons to increasing sucrose concentrations under both WR and FR. However, the dynamics of these signals across sucrose concentrations differed markedly between WR and FR in sg*Rosa26* control mice but were largely similar in sg*Trpc6* mutant mice. Results observed in *sgRosa26* control mice are consistent with findings that DA neurons differentially encode information relating to hydration and caloric intake under thirst and hunger conditions (Grove et al., 2022). These results suggest that TRPC6 channel activation, likely downstream of specific neuropeptide receptors, functions in a state-dependent manner.

Our *in vivo* results also demonstrate a broader range of value encoding in sg*Rosa26* control mice—but not *sgTrpc6* mice—under FR compared to WR, suggesting differential activation of neuropeptide receptors that are coupled to TRPC6 channels. The neuropeptides that recruit activation of TRPC6 channels in hungry mice are not yet known, but candidates include NTS, which has been shown to regulate feeding (Gazit Shimoni et al., 2025; Ramirez-Virella & Leinninger, 2021), and the gut-derived peptide ghrelin that is also $G_{q/11}$ coupled and enhances dopamine neuron activity (Abizaid et al., 2006). In contrast, DA responses to thirst are regulated by renin/angiotensin signaling, but this effect is thought to be mediated by angiotensin II receptor signaling outside the VTA (Hsu et al., 2020). Future studies will explore the mechanisms by which neuropeptide inputs to VTA-DA neurons modulate TRPC6 channel activation in a homeostatic state-dependent manner.

In conclusion, our findings support previous work illustrating how neuropeptide receptor activation of TRPC channels tightly regulates neuronal excitability and synchronized activity (Kelly and Wagner, 2024). We demonstrate a novel mechanism by which TRPC6 channels are coupled to neuropeptidergic signaling pathways to regulate VTA-DA neuron activity and behavior under specific homeostatic demands. Current studies are characterizing TRPC6 channel-dependent synchronized calcium dynamics in VTA-DA neurons at single-cell resolution *in vivo*.

Importantly, our electrophysiological data confirm that the differences we observe in calcium signaling after *Trpc6* mutagenesis are not due to changes in intrinsic or evoked excitability. The lack of effect on baseline neuronal properties underscores the therapeutic potential of TRPC6 channels, as interventions targeting these channels could modulate pathological signaling without disrupting essential neuronal function. These results provide evidence for TRPC6 channels as a potential therapeutic target for a variety of disorders related to imbalances in consummatory and reward-related behaviors.

2.4 Methods

Male and female mice, housed on a 12-h light/dark cycle, were used in all experiments performed during the light phase. All procedures were approved and performed under the guidelines of the Institutional Animal Care and Use Committee at the University of Washington (PROTO201600703 – 4249-01). Mice between the ages of 2–6 months were used for all experiments. DAT-Cre mice (B6.SJL-*Slc6a3*$^{tm1.1(cre)Bkmn}$/J) were purchased from The Jackson Laboratory and bred in-house.

Viruses

All AAV1 viruses were produced in-house with titers of 1×10^{12} to 3×10^{12} particles per mL as described (Gore et al., 2013).

Design of CRISPR Constructs

Primers used for cloning sg*Trpc6*(1) into AAV1-FLEX-SaCas9-U6 were: forward CACCGAGCCTTTAGAGAGCCGCCCCT and reverse AAACAGGGGCGGCTCTCTAAAGGCTC. Primers used for cloning sg*Trpc6*(2) into AAV1-FLEX-SaCas9-U6 were: forward CACCGTCCTACTACATTGGCGCAAAA and reverse AAACTTTTGCGCCAATGTAGTAGGAC. The control CRISPR virus used was AAV1-FLEX-SaCas9-U6-sg*Rosa26,* and single-guide RNAs targeting *Trpc6* were designed as previously published (Hunker et al., 2020; Hunker and Zweifel, 2020). All CRISPR viruses contained a hemagglutinin (HA) tag used to confirm virus expression using immunohistochemistry.

Validation of Mutagenesis

Validation of mutagenesis was performed using fluorescence-activated cell sorting, whole-genome amplification and sequencing as described (Hunker et al., 2020; Hunker & Zweifel, 2020). In brief, three DAT-Cre mice were injected in the VTA with AAV1-FLEX-SaCas9-U6-sg*Trpc6*(1) and AAV1-FLEX-SaCas9-U6-sg*Trpc6*(2) along with AAV-FLEX-EGFP-KASH to label nuclei for sorting. Four weeks following injection tissue punches of the VTA were collected and GFP-positive nuclei were isolated using fluorescence-activated cell sorting. Whole-genome amplification (REPLI-g, Qiagen) was performed according to the manufacturer's instructions, followed by targeted sequencing of a 200–300 bp region surrounding the intended cut site. Tracking of indels by decomposition (TIDE) analysis (Brinkman et al., 2014) was performed to compare sequence chromatograms from GFP-negative and GFP-positive samples to estimate mutation frequency.

Surgery

Mice were anesthetized with isoflurane (1.5–4%) before and during viral injections and fiber implantations. Mice recovered for at least 4 weeks prior to experimentation. For slice electrophysiology, mice were injected at approximately 5–6 weeks of age. For all other experiments, mice were injected at 8–12 weeks of age. VTA coordinates were M–L: ±0.5, A–P: −3.25, D–V: −4.4. Values are in mm, relative to bregma. A–P values were adjusted for bregma–lambda distance using a correction factor of 4.21 mm. For z-values the syringe was lowered 0.5 mm past the indicated depth and raised up at the start of the injection. Injection volume was 500 nL at a rate of 250 nL/min. All injections were bilateral.

For electrophysiology and *ex vivo* calcium imaging experiments, all mice were injected with AAV1-FLEX-GCaMP8f at a 1:4 dilution. The diluent was the CRISPR virus: AAV1-FLEX-sg*Rosa26* (control) or AAV1-FLEX-sg*Trpc6*(1) and AAV1-FLEX-sg*Trpc6*(2) (experimental group). For fiber photometry experiments, all mice were injected with AAV1-FLEX-GCaMP6m at a 1:6 dilution. The diluent was the CRISPR virus: AAV1-FLEX-sg*Rosa26* (control) or AAV1-FLEX-sg*Trpc6*(1) and AAV1-FLEX-sg*Trpc6*(2) (experimental group).

Fiber-optic cannulas for photometry (400 µm fiber, 0.66 NA, 1.25 mm ferrule) were purchased from Doric and implanted in the VTA at a depth of −4.2 mm from bregma. Implantations were unilateral and implanted in the left hemisphere.

***Ex Vivo* Slice Physiology**

Horizontal brain slices (200 µm) were prepared in artificial cerebrospinal fluid (ACSF) solution 32 °C containing (in mM): 126 NaCl, 2.5 KCl, 1.2 $MgCl_2$, 2.4 $CaCl_2$, 1.2 NaH_2PO_4, 21.4 $NaHCO_3$, 11.1 D-glucose and 10 µM MK-801 (to prevent NMDA-mediated excitotoxicity). Slices recovered in ACSF (in mM: 126 NaCl, 2.5 KCl, 1.2 NaH_2PO4, 1.2 $MgCl_2$ 11 d-glucose, 18 $NaHCO_3$, 2.4 $CaCl_2$) at 32°C containing 10 µM MK-801 for ≥ 30 minutes. All solutions were continually bubbled with O_2 and CO_2.

Slices were hemisected along the midline, and one half was transferred to a recording chamber under continuous perfusion (~2 ml min^{-1}) of oxygenated ACSF at 32 °C while the other was placed back into recovery. Recordings began in a whole-cell voltage clamp configuration with glass microelectrodes (World Precision Instruments) with a resistance of 2-3 MΩ. All electrophysiology experiments used an internal solution containing (in mM): 130 K-gluconate, 10 HEPES, 5 NaCl, 1 EGTA, 5 Mg-ATP, 0.5 Na-GTP, pH 7.3, 280 mOsm. Once a stable recording was achieved at -60 mV, cells were switched to current clamp and the spontaneous activity that followed for the next 70 seconds was recorded. Cells were then given escalating current steps (Δ = +10 pA) from -60 pA to +230 pA. Finally, cells were given a ramp protocol from 0 to 200 pA over 2 seconds. Basal electrical properties were measured and monitored following break-in using the average of eight 5 mV pulses (10 ms pulse, sampled at 10 kHz). Cells with a series resistance ≥16 MΩ, or with a change in series resistance ≥50% during the recording period were excluded from analysis. Whole-cell recordings were made using an Axonpatch 700B amplifier (Molecular Devices) and Clampex software.

Electrophysiology Data Analysis

Electrophysiological data were acquired using Clampex software and analyzed post hoc with custom Python scripts. Recordings consisted of single or multiple sweeps loaded with the Neo library and AxonIO module. Spontaneous action potentials were detected by calculating the first derivative of voltage (dV/dt) and applying a threshold of ≥15 mV/ms. To quantify spontaneous firing rates, a sliding window analysis (10-second duration) was performed to identify the highest frequency of spontaneous action potentials within a 70-second recording period.

Resting membrane potential was estimated by identifying interspike intervals of at least 200 ms and calculating the average voltage over a 50-point window within these quiescent periods. This approach ensured that measurements reflected the membrane's most hyperpolarized state and were not influenced by pre-spike depolarizations or post-spike afterpotentials.

Spike width was determined by identifying action potential boundaries: the spike onset was defined as the first point before the detected peak where $dV/dt \leq 0$, and repolarization was identified as the point following the peak where dV/dt returned to ≥ 0. Spike width was subsequently measured between these two boundary points. The coefficient of variability (CV) of inter-spike intervals (ISI) was calculated to assess firing regularity.

Additionally, rheobase currents were determined from ramp current injections by calculating the minimum current required to elicit an action potential using robust spike validation criteria. Spikes during ramp protocols were validated based on sustained threshold crossing of dV/dt (≥ 0.1× peak dV/dt for ≥ 0.5 ms) and confirmed depolarization above 0 mV. The spike threshold voltage was defined as the membrane potential at the first point of dV/dt threshold crossing that led to a full action potential and was used to quantify the voltage level at which each neuron initiated firing.

Ex Vivo Slice Calcium Imaging

Horizontal brain slices (200 µm) were prepared in an ice slush solution containing (in mM): 92 *N*-methyl-d-glucamine, 2.5 KCl, 1.25 NaH_2PO4, 30 $NaHCO_3$, 20 HEPES, 25 glucose, 2 thiourea, 5 sodium ascorbate, 3 sodium pyruvate, 0.5 $CaCl_2$, 10 $MgSO_4$, pH 7.3–7.4 (Ting, 2014). Slices recovered for 12 minutes in the same solution at 32 °C and then were transferred to a room temperature solution including (in mM): 92 NaCl, 2.5 KCl, 1.25 NaH_2PO_4, 30 $NaHCO_3$, 20 HEPES, 25 glucose, 2 thiourea, 5 sodium ascorbate, 3 sodium pyruvate, 2 $CaCl_2$, 2 $MgSO_4$. Slices recovered for an additional 45 minutes before recordings were made in ACSF at 32 °C that was continually perfused over slices at a rate of ~2 ml min^{-1} and contained (in mM): 126 NaCl, 2.5 KCl, 1.2 NaH_2PO4, 1.2 $MgCl_2$ 11 d-glucose, 18 $NaHCO_3$, 2.4 $CaCl_2$. All solutions were continually bubbled with O_2 and CO_2.

For bath application experiments, a 3-minute baseline period was recorded. Senktide (500 nM) was applied for two minutes, then a 10-minute washout period followed. For puffing experiments, ~10 MΩ electrodes were filled with either GSK 1702934A (1 µM and 300 nM), (S)-3,5-Dihydroxyphenylglycine (30 µM), neurotensin (1 µM), senktide (500 nM), or carbachol (30 µM) diluted with an internal solution (in mM): 126 NaCl, 2.5 KCl, 1.2 NaH_2PO_4, 1.2 $MgCl_2$ 11 d-glucose, 18 $NaHCO_3$, 2.4 $CaCl_2$.

The puffing pipette was situated adjacent to the cell of interest, and only one cell was analyzed per puff. Only cells that exhibited a visual mechanical deflection in response to the puff were subsequently analyzed. Importantly, while this deflection was reflected by a sharp negative trough in the calcium signal, the calcium signal immediately rebounded. Cells that exhibited a deflection and an increase in calcium signal were classified as responders; cells that exhibited the deflection without increase in calcium fluorescence were categorized as nonresponders (see Fig. 1H inset for an example). Images were acquired using a high-speed camera (Hamamatsu OrcaFlash 4.0LT) and Metafluor software.

Ex Vivo Slice Calcium Imaging Data Analysis

ΔF/F was calculated from the 3-minute baseline period using ImageJ and Inscopix software. Peak fluorescence and area under the curve were compared between the two groups using a Student's t-test.

Fiber Photometry

Mice were connected to an imaging patch cord (Doric Lenses) and head-fixed in the multi-spout apparatus. The imaging patch cord was photobleached for 10 minutes prior to recording. Recordings were made using an RZ5 BioAmp Processor and Synapse software (Tucker Davis Technologies). A 465 nm LED (531-Hz, sinusoidal, Doric Lenses) was used to excite GCaMP6m. LED intensity was measured at the tip of the optic fiber prior to each recording session and set to 30–40 μW. GCaMP6m fluorescence (525 ± 25 nm) was returned through the same patch cord, bandpass filtered, and recorded by the RZ5 at a sampling rate of 1,017.25 Hz. Spout extension events were synced to the photometry recording via TTL delivery for offline analysis.

Fiber Photometry Data Analysis

The 465 nm signal was preprocessed as previously described (Simpson et al., 2024). In brief, the signal was down sampled 100x using a moving window mean and corrected for photobleaching using a double exponential curve fit and subtraction (Simpson et al., 2024). A custom Python package adapted from the Tucker Davis code was used to extract and analyze the GCaMP signal surrounding each event. A 30-second window was extracted surrounding each spout extension (10 seconds prior and 20 seconds following). Five seconds to one second prior to spout extension was used as a baseline to calculate the z-score. Z-scores for each unique spout identity were averaged for each mouse.

Multi-spout Apparatus

Mice were head-fixed in an OHRBETS (Open-Source Head-fixed Rodent Behavioral Experimental Training System) as described (Gordon-Fennell et al., 2023). Briefly, OHRBETS was constructed from 3D printed components and Arduino hardware. Mice were trained to lick for solutions from multiple rotating and retracting spouts. Under water restriction, mouse weights were held consistent at 90% baseline. Under food restriction, mouse weights were held consistent at 85% of baseline weight. Multi-spout experiments were completed in four cohorts of mice.

Habituation to Head Fixation and Free-access Lick Training

Mice were water restricted to 90% baseline weight. Mice were habituated to head fixation and trained to lick for 10% sucrose in a single 10-minute session. Mice were scruffed and gently had their rear end and hind paws placed in a 50 mL conical during head fixation. During this session, mice were given free access to 10% sucrose. Free access was approximated using closed-loop delivery of a pulse of fluid (~1.5 μL) each time the mouse licked the spout. The spout was positioned ~2–3 mm in front of the mouse’s mouth where it remained throughout the session (Gordon-Fennell et al., 2023).

Retractable Spout Training

Mice were water restricted to 90% of baseline weight. Retractable spout training consisted of two daily sessions of 60 trials using one spout. The trial structure was as follows: spout extension, one second delay with no liquid available, 3 seconds of free access of 10% sucrose as described above, a one second delay with no liquid delivery, spout retraction. The inter-trial interval was a variable 15-20 seconds.

Multi-spout Brief Access Sucrose Experiment

Mice were either food-restricted or water-restricted. Mice underwent five consecutive days of multi-spout brief access for five concentrations of sucrose (0%, 5%, 10%, 20%, 30%) across 60 trials. The trial structure was as follows: spout extension, one second delay with no liquid available, 3 seconds of free access of 10% sucrose, a one second delay with no liquid delivery, spout retraction. The inter-trial interval was a variable 15-20 seconds. Each spout contained a different concentration of sucrose that remained the same throughout the daily session. The solutions in the spouts, as well as the order of the spout presentations, were pseudorandomly assigned each day. Fiber photometry signals were recorded during the third, fourth and fifth days of the experiment. Licking and photometry data are presented as the average of these three days for each mouse.

Immunohistochemistry

Mice were deeply anesthetized using Beuthanasia and transcardially perfused with phosphate-buffered saline (PBS), followed by 4% paraformaldehyde (PFA) in PBS. Brains were placed in 4% PFA overnight, then transferred to 30% sucrose in PBS solution at 4°C for at least 48 hours. Brains were then sectioned into 45µm sections using a cryostat and placed in PBS at 4°C. Brain sections were then stained to validate virus expression. Free-floating sections were placed in a blocking buffer (3% normal donkey serum and 0.3% Triton X-100 in PBS) for 30 minutes. For enhancement of GCaMP6m and HA tag, sections were incubated in primary antibodies (Chicken-GFP, 1:6000 dilution, ABCAM, Rabbit-HA, 1:1000) overnight at 4°C. Sections were then placed in PBS for three 10-minute washes and incubated in secondary antibody (1:250 dilution Alexa Fluor 488 AffiniPure Donkey Anti-Chicken or Cy3 Donkey Anti-Rabbit, Jackson ImmunoResearch) for 45 minutes at room temperature. Then, following three 10-minute PBS washes, sections were mounted using a mounting medium (DAPI Fluoromount-G, Southern Biotech) and cover-slipped. Images were collected using a Keyence BZ-X710 fluorescent microscope and analyzed using ImageJ software.

Statistics and Reproducibility

All data were analyzed for statistical significance using Prism software (GraphPad Prism 9). No statistical methods were used to predetermine sample sizes. All behavioral assays were repeated in a minimum of two cohorts with similar replication of results. Littermates were randomly assigned to experimental groups and mice were tested in random order. Mice with missed viral injections or significant viral spread outside the targeted region were excluded from analyses. A complete list of statistical tests can be found in Extended Data Table 1.

Acknowledgments

This work was supported by National Institutes of Health grants R01MH104450 (LSZ), R01DA044315 (LSZ), and F31DA058381 (MXB). We thank Dr. Selena Schattauer for assistance with viral production and the FACS experiment, as well as the University of Washington Center of Excellence in Opioid Addiction Research/Molecular Genetics Resource Core (P30DA048736). We thank Dr. Marta Soden and Mary Loveless for assistance with the multi-spout apparatus. We also thank members of the Zweifel, Soden, and Palmiter labs for their thoughtful discussions.

Author contributions

M.X.B. and L.S.Z. conceptualized the project and experimental design for all experiments. M.X.B. acquired the puff slice calcium imaging and fiber photometry datasets. M.T. collected the bath application slice calcium imaging dataset. O.K. collected and analyzed the electrophysiology datasets. M.X.B. and D.T.M. wrote Python scripts and analyzed all the datasets. A.F. and L.S.Z. assisted with additional data analyses. S.J. aided with construction of the multi-spout apparatus and provided thoughtful discussion. M.X.B. and L.S.Z wrote the manuscript. All authors reviewed the manuscript.

Competing Interests

The authors have no competing interests to declare.

Code Availability

Code for fiber photometry analysis was derived from a publicly available source (Tucker Davis Technologies) and is available through GitHub (https://github.com/molliebernstein).

2.5 Figures and legends for Chapter 2

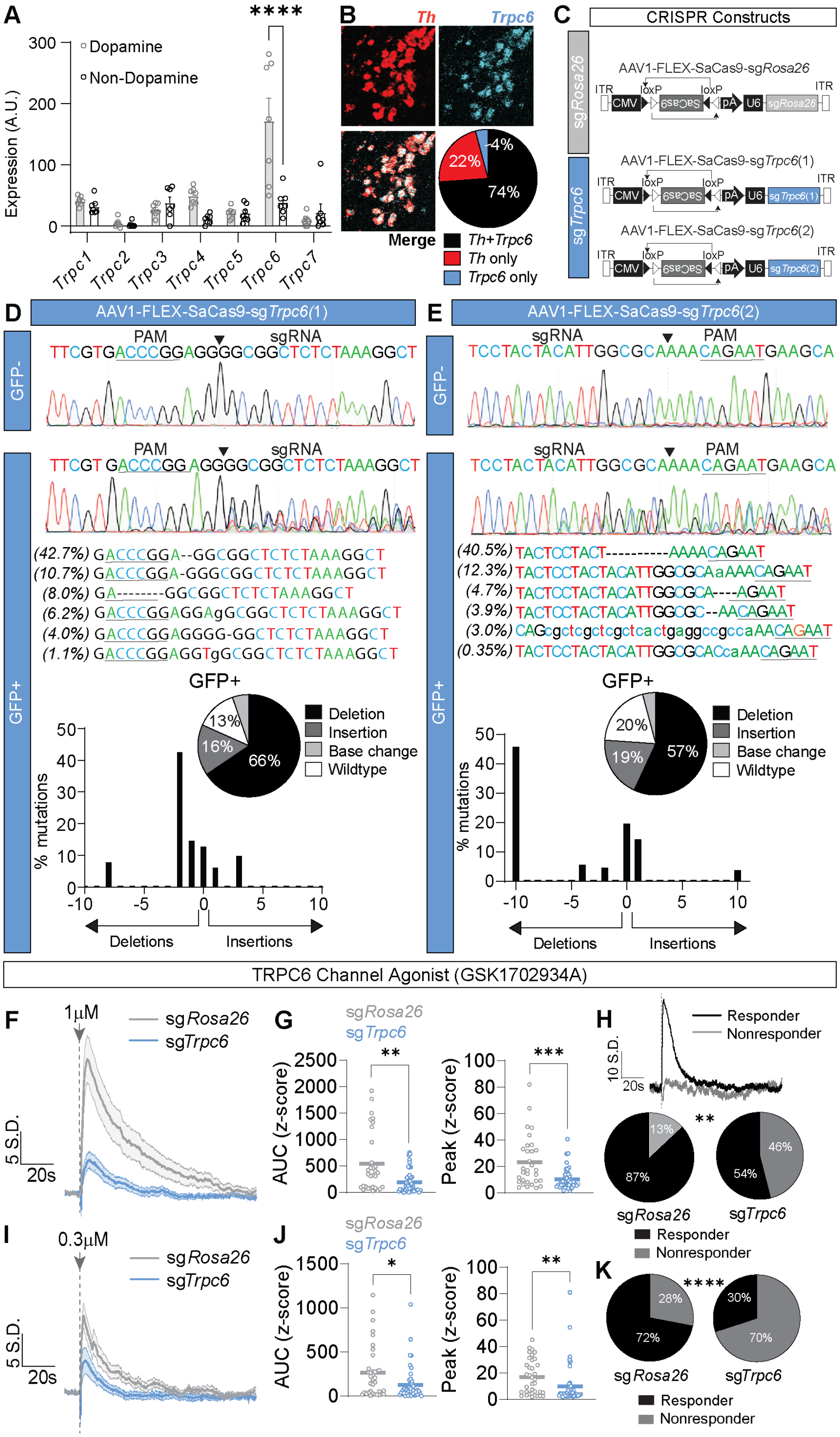

Figure 1. Validation of *Trpc6* mutagenesis approach. (A) mRNA expression of TRPC channel-encoding genes in the VTA of adult mice adapted from Chung et al. (2017) (N=7 mice; Two-way repeated measures ANOVA followed by Bonferroni post hoc comparison, ****P<0.0001). (B) *In situ* hybridization experiment showing localization of *Th, Trpc6,* and co-localization of *Th* and *Trpc6* (N=3 mice, n=3 hemi sections/mouse). (C) Schematic showing the CRISPR constructs injected into the sg*Rosa26* (control) and sg*Trpc6* (experimental) groups. (D, E) Quantification of mutagenesis in the *Trpc6* gene in VTA-DA GFP- and GFP+ cells in AAV1-FLEX-SaCas9-sg*Trpc6*(1) injected mice (N=3 mice) (D) and AAV1-FLEX-SaCas9-sg*Trpc6*(2) injected mice (N=3 mice) (E). Dashed lines indicate nucleotide deletions; lowercase letters indicate nucleotide insertions. (F-K) *Ex vivo* slice calcium imaging experiment of VTA-DA cells with a 50 ms puff application of TRPC6 channel direct agonist GSK1702934A at 1 µM (F-H) and 0.3 µM (I-K). Mean ± S.E.M. z-score traces (F, I), AUC and peak analyses for 1 µM (G) and 0.3 µM (J). (H, K) Responder classification analysis for both concentrations; example trace of both types are shown in the top panel of (H). (G-H) (N= 4 sg*Rosa26* mice, n=31 cells and N= 3 sg*Trpc6* mice, n=46 cells; D'Agostino & Pearson Test, Mann Whitney, Chi-squared test, **P<0.01, ***P<0.001). (J-K) (N= 3 sg*Rosa26* mice, n=36 cells and N= 3 sg*Trpc6* mice, n=47 cells; D'Agostino & Pearson Test, Mann Whitney, Chi-squared test, *P<0.05, **P<0.01, ****P<0.0001). See Extended Data Table 1 for details on statistical tests.

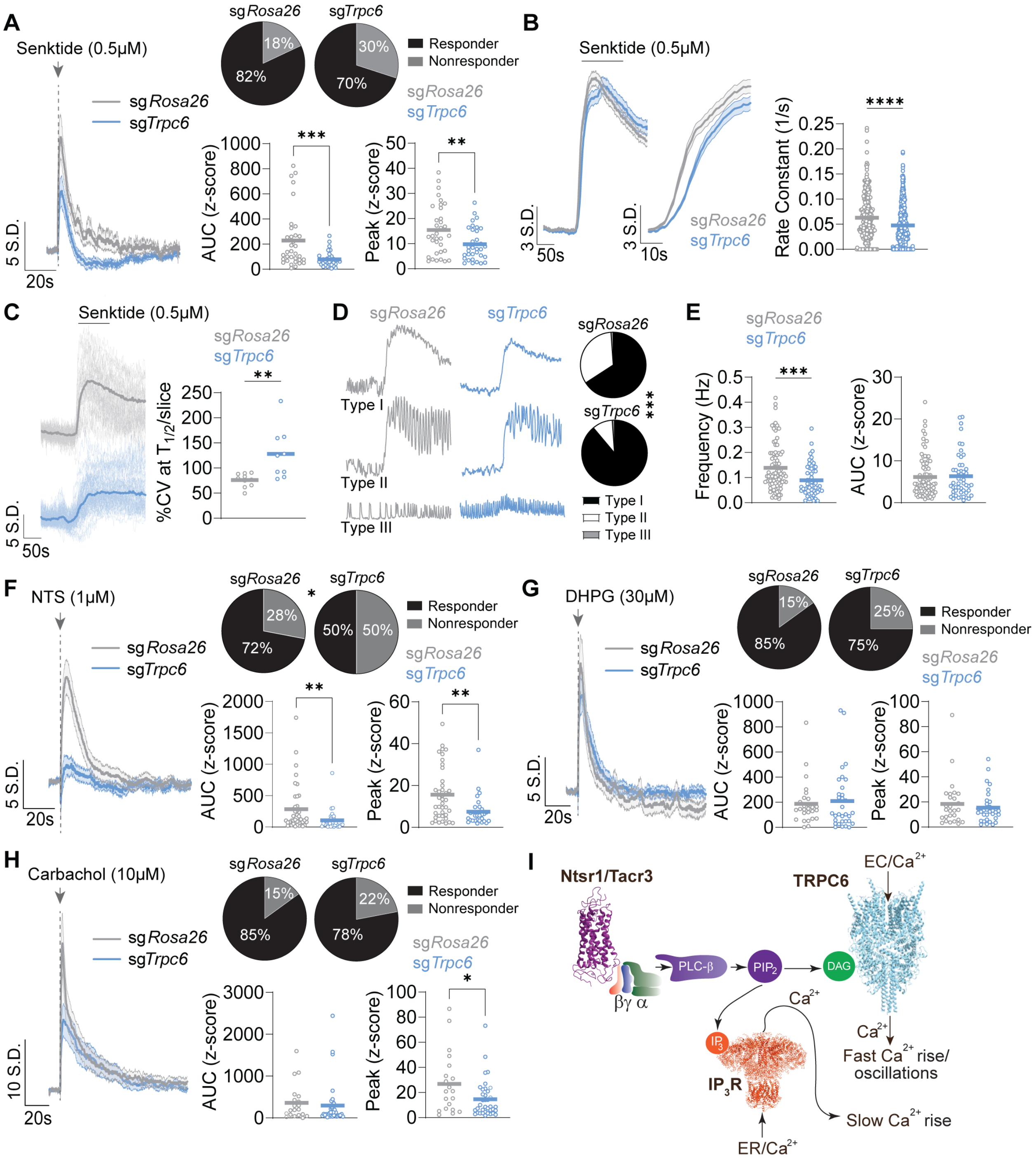

Figure 2. TRPC6 channels are coupled to neuropeptide receptor signaling pathways. (A) *Ex vivo* slice calcium imaging experiment of VTA-DA cells following a 50 ms puff application of senktide (0.5 µM) with mean ± S.E.M. z-score traces, AUC, peak, and responder classification analyses (N=4 sg*Rosa26* mice, n=34 cells and N=4 sg*Trpc6* mice, n=33 cells; D'Agostino & Pearson Test,

Mann Whitney, Chi-squared test, **P<0.01, ***P<0.0001). (B-E) *Ex vivo* slice calcium imaging experiment of VTA-DA cells following a 5 min bath application of senktide (0.5 μM). (B) Average rise (left panel), initial rise (middle panel) and rate constant analysis (right panel) for the initial rise time of calcium fluorescence (N=3 sg*Rosa26* mice*,* n=290 cells and N=3 sg*Trpc6* mice, n=512 cells; Independent t-test, ****P<0.0001). (C) Data from one slice per group from (B) where the solid line is the average trace (left panel); coefficient of variation (CV), expressed as a percentage, taken at $T_{1/2}$ per slice (right panel) (N=3 sg*Rosa26* mice, n=10 slices and N=3 sg*Trpc6* mice, n=9 slices; Independent t-test, **P<0.01). (D) Example traces for Type I, II, and III responsive cells (left panel) and proportion analysis (right panel) (Fisher's exact test, ***P<0.001). (E) Frequency of oscillations for Type II and III cells (left panel) and AUC analysis (right panel) (N=3 sg*Rosa26* mice, n=84 cells and N=3 sg*Trpc6* mice, n=52 cells; D'Agostino & Pearson Test, Mann Whitney, ***P<0.001). (F) *Ex vivo* slice calcium imaging experiment of VTA-DA cells with a 50 ms puff application of neurotensin (NTS) (1 μM) with mean ± S.E.M. z-score traces, AUC, peak, and responder classification analyses (N= 3 sg*Rosa26* mice, n=40 cells and N= 3 sg*Trpc6* mice, n=30 cells; D'Agostino & Pearson Test, Mann Whitney, Chi-squared test, *P<0.05, **P<0.01). (G) *Ex vivo* slice calcium imaging experiment of VTA-DA cells with a 50 ms puff application of (S)-3,5-Dihydroxyphenylglycine (DHPG) (30 μM) with mean ± S.E.M. z-score traces, AUC, peak, and responder classification analyses (N= 3 sg*Rosa26* mice, n=27 cells and N=3 sg*Trpc6* mice, n=32 cells; D'Agostino & Pearson Test, Mann Whitney, Chi-squared test). (H) *Ex vivo* slice calcium imaging experiment of VTA-DA cells with a 50 ms puff application of carbachol (10 μM) with mean ± S.E.M. z-score traces, AUC, peak, and responder classification analyses (N=3 sg*Rosa26* mice, n=20 cells and N=4 sg*Trpc6* mice, n=37 cells; D'Agostino & Pearson Test, Mann Whitney, Chi-squared test, *P<0.05). (I) A model by which activation of neurotensin receptor 1 (Ntsr1) and tachykinin receptor 3 (Tacr3) initiates a signaling cascade resulting in extracellular (EC) Ca^{2+} ions flowing into the cell through TRPC6 channels contributing to a fast rise in [Ca^{2+}] and Ca^{2+} oscillations. Ca^{2+} ions exit the endoplasmic reticulum (ER) via IP_3 receptors giving rise to a slow rise in [Ca^{2+}]. IP_3 = inositol trisphosphate, PLC-β = phospholipase C beta, PIP_2 = phosphatidylinositol bisphosphate, DAG = diacylglycerol. See Extended Data Table 1 for details on statistical tests.

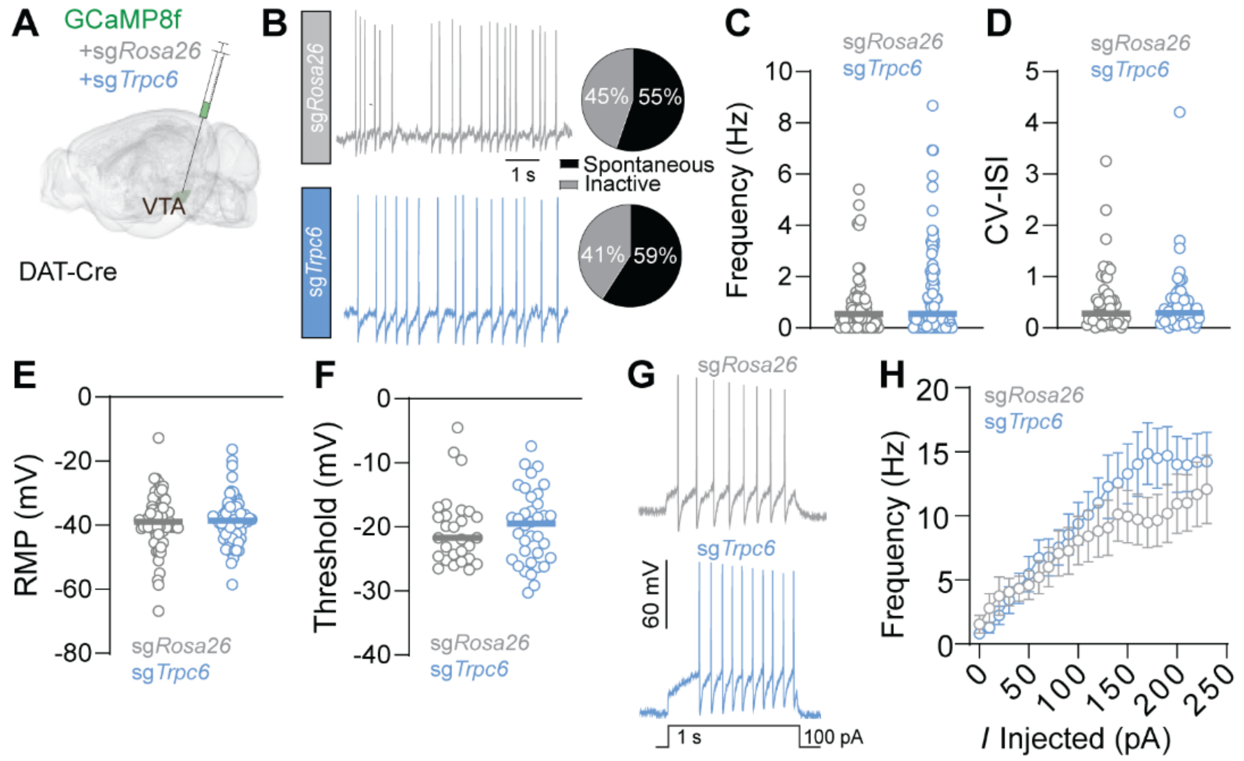

Figure 3. *Trpc6* mutagenesis does not alter spontaneous or evoked action potential firing in dopamine neurons. (A) Schematic illustrating viral injection into the VTA of DAT-Cre mice. (B) Representative traces of spontaneous action potential firing in sg*Rosa26* and sg*Trpc6* injected mice. The proportion of spontaneously active versus inactive cells did not differ significantly (N=5 sg*Rosa26* mice, n=76 cells and N=6 sg*Trpc6* mice, n=66 cells, Fisher's exact test, P=ns). (C) Spontaneous firing frequency in sg*Rosa26* and sg*Trpc6* injected mice did not differ significantly (N=5 sg*Rosa26* mice, n=65 cells and N=6 sg*Trpc6* mice, n=80 cells; D'Agostino & Pearson Test, Mann Whitney, P=ns). (D) Coefficient of variation in the interspike interval (CV-ISI) in sg*Rosa26* and sg*Trpc6* injected mice did not differ significantly (N=5 sg*Rosa26* mice, n=51 cells and N=6 sg*Trpc6* mice, n=56 cells; D'Agostino & Pearson Test, Mann Whitney, P=ns). (E) Resting membrane potential (RMP) in sg*Rosa26* and sg*Trpc6* injected mice did not differ significantly (N=5 sg*Rosa26* mice, n=65 cells and N=6 sg*Trpc6* mice, n=67 cells; D'Agostino & Pearson Test, Mann Whitney, P=ns). (F) Threshold to fire action potential during ramp current injection in

sg*Rosa26* and sg*Trpc6* injected mice did not differ significantly (N=8 sg*Rosa26* mice, n=28 cells and N=3 sg*Trpc6* mice, n=36 cells; D'Agostino & Pearson Test, Mann Whitney, P=ns). (G) Example traces following current injection in sg*Rosa26* and sg*Trpc6* injected mice. (H) Spikes fired following current injection did not differ between sg*Rosa26* and sg*Trpc6* injected mice (N=13 sg*Rosa26* mice, n=15 cells and N=9 sg*Trpc6* mice, n=26 cells; Two-way repeated measures ANOVA, Bonferroni's multiple comparisons, P=ns). Data are presented as the mean ± S.E.M.

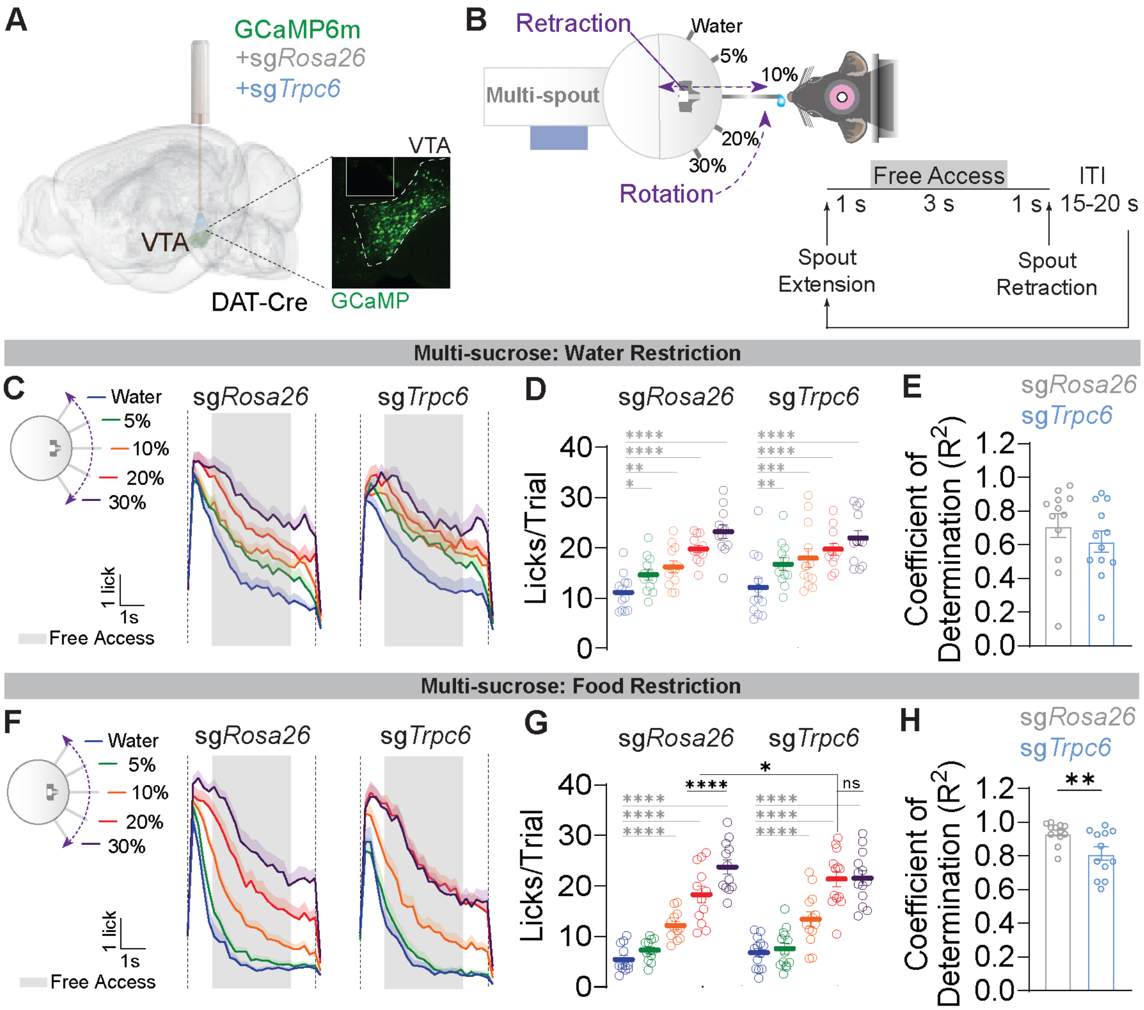

Figure 4. TRPC6 channels modulate licking behavior in a multi-sucrose consumption task under food restriction but not water restriction. (A) Schematic illustrating viral injections and optic fiber implants in the VTA of DAT-Cre mice. Inset is a representative histology image from immunohistochemistry validation of targeting. (B) Schematic of the OHRBETS system and trial structure that consists of a rotating and retracting five-spout apparatus. Head-restrained mice are presented with one spout at a time. Spout extension is followed by a 1 sec delay, 3 sec free access delivery of liquid, 1 sec delay, spout retraction, then a variable 15-20 sec inter-trial interval (ITI). (C-E) Multi-sucrose experiment under 90% water restriction. Lick rate graphs (C) and quantification of total licks per trial (D) for each spout identity (N=12 mice for both groups; Two-

way repeated measures ANOVA, Tukey's multiple comparisons, *P<0.05, **P<0.01, ***P<0.001, ****P<0.0001). (E) Regression coefficient analysis per animal (N=12 mice for both groups; Independent t-test, P=ns). (F-H) Multi-sucrose experiment under 85% food restriction. Lick rate graphs (F) and quantification of total licks per trial (G) for each spout identity (N=12 mice for both groups; Two-way repeated measures ANOVA, Tukey's multiple comparisons, *P<0.05, ****P<0.0001). (H) Regression coefficient analysis per animal (N=12 mice for both groups; Independent t-test, **P<0.01). See Extended Data Table 1 for details on statistical tests. Data are presented as the mean ± S.E.M. averaged across three days of the experiment for C-H.

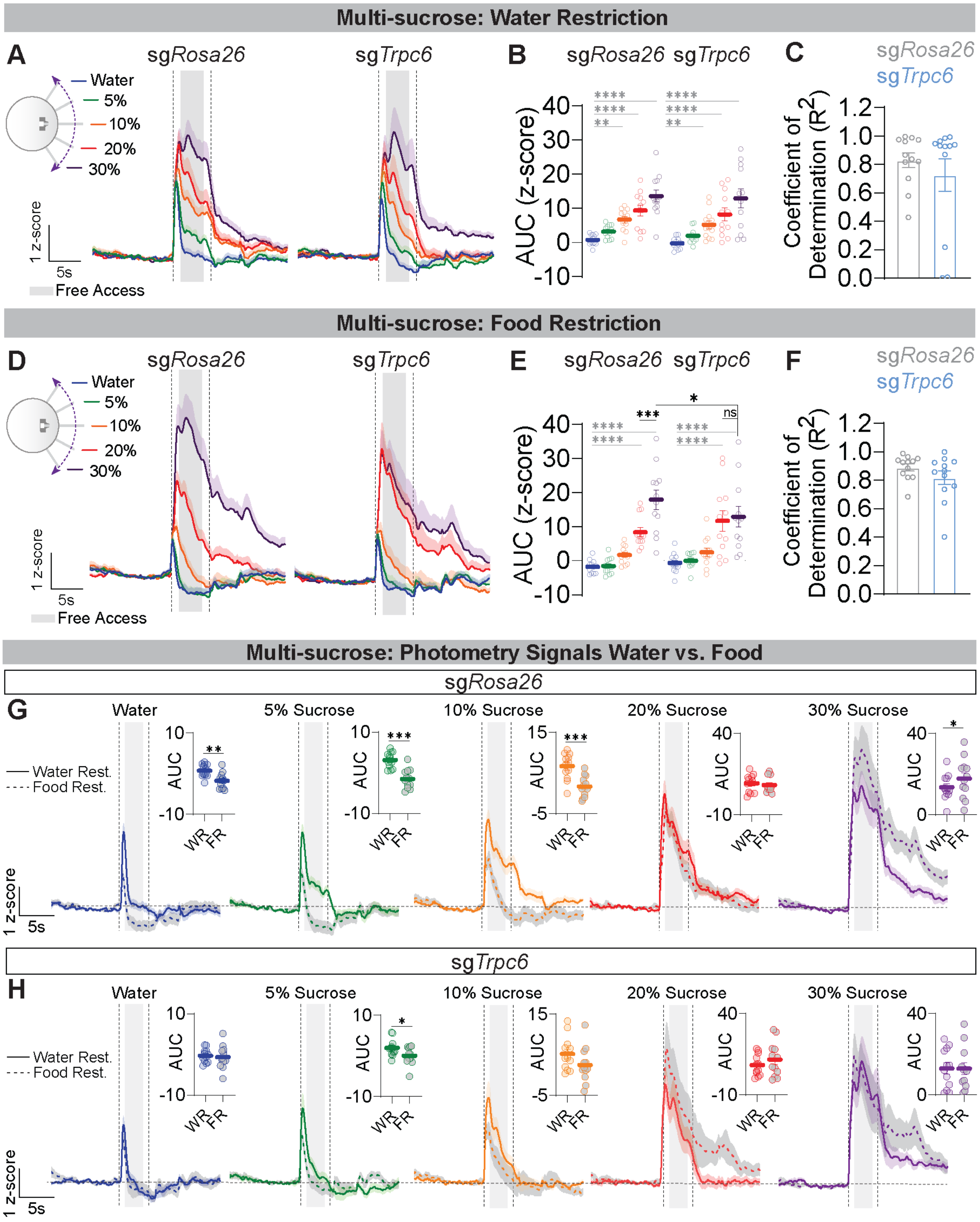

Figure 5. TRPC6 channels regulate *in vivo* VTA-DA calcium signals during a multi-sucrose consumption task under food restriction but not water restriction. (A-C) Multi-sucrose experiment under 90% water restriction. Z-scored fiber photometry signals aligned to spout extension (A) and

AUC quantified during the 3 sec free access period (B) for each spout identity (N=12 mice for both groups; Two-way repeated measures ANOVA, Tukey's multiple comparisons, **P<0.01, ****P<0.0001). (C) Regression coefficient analysis per animal (N=12 mice for both groups; Independent t-test, P=ns). (D-F) Multi-sucrose experiment under 85% food restriction. Z-scored fiber photometry signals aligned to spout extension (D) and AUC quantified during the 3 sec free access period (E) for each spout identity (N=12 mice for both groups; Two-way repeated measures ANOVA, Tukey's multiple comparisons, *P<0.05, ***P<0.001, ****P<0.0001). (F) Regression coefficient analysis per animal (N=12 mice for both groups; Independent t-test, P=ns). Comparisons of z-scored fiber photometry signals and AUC quantifications from A, B, D, E between water restriction and food restriction experiments for each spout identity for sg*Rosa26* mice (G) and sg*Trpc6* mice (H) (N=12 mice for both groups; Paired samples t-test, *P<0.05, **P<0.01, ***P<0.001). See Extended Data Table 1 for details on statistical tests. Data are presented as the mean ± S.E.M. averaged across three days of the experiment for A-H.

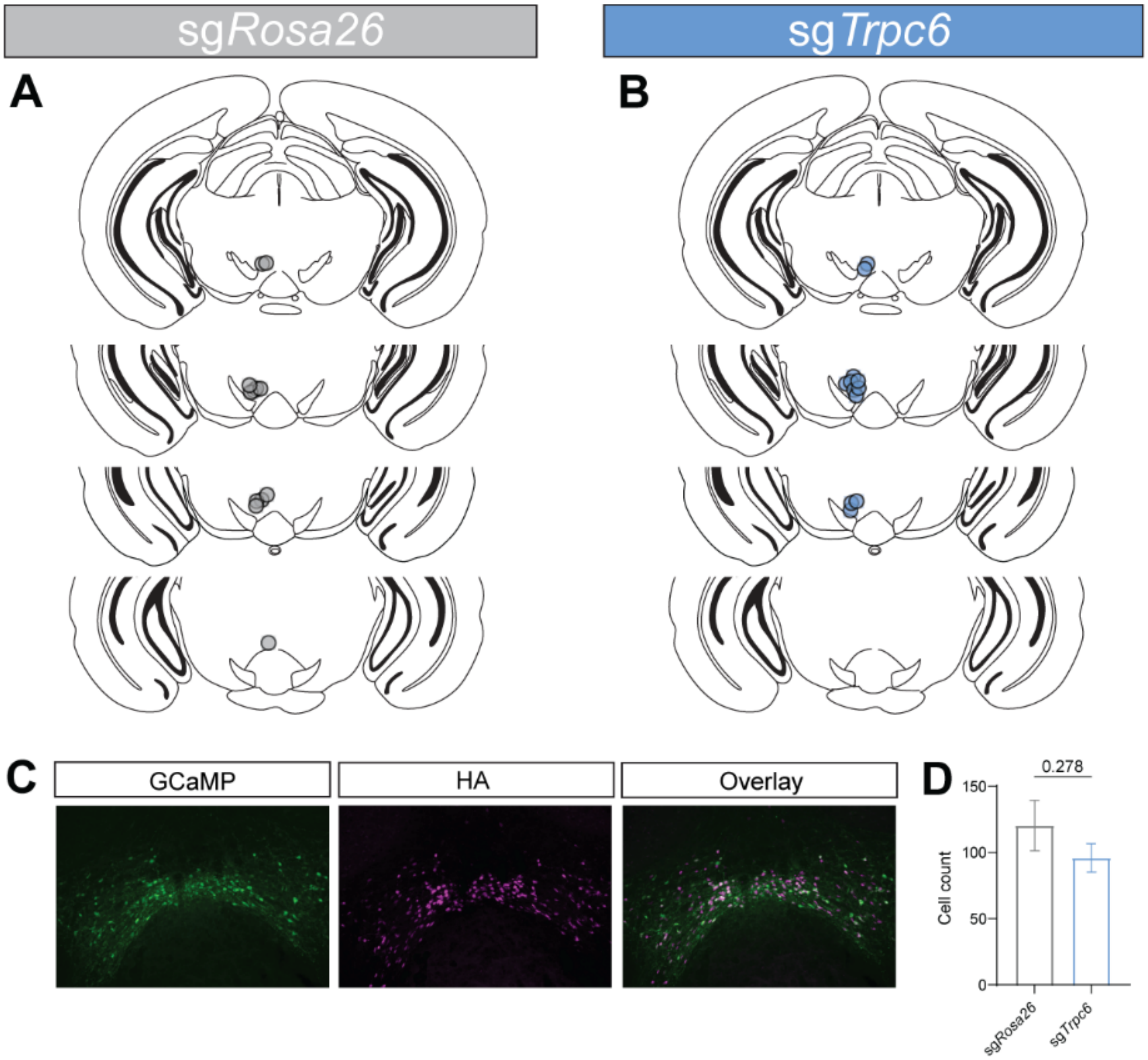

Supplemental Figure 1. Histological validation for fiber photometry mice. Optic fiber placements in the VTA for sg*Rosa26* mice (A) and sg*Trpc6* mice (B) (N=12 mice for both groups). (C) Representative immunohistochemistry images showing co-expression of GCaMP and hemagglutinin (HA) (CRISPR virus expression). (D) Cell counts for GCaMP positive cells from fiber photometry mice in A and B (N=12 mice for both groups; Independent t-test, P=ns).

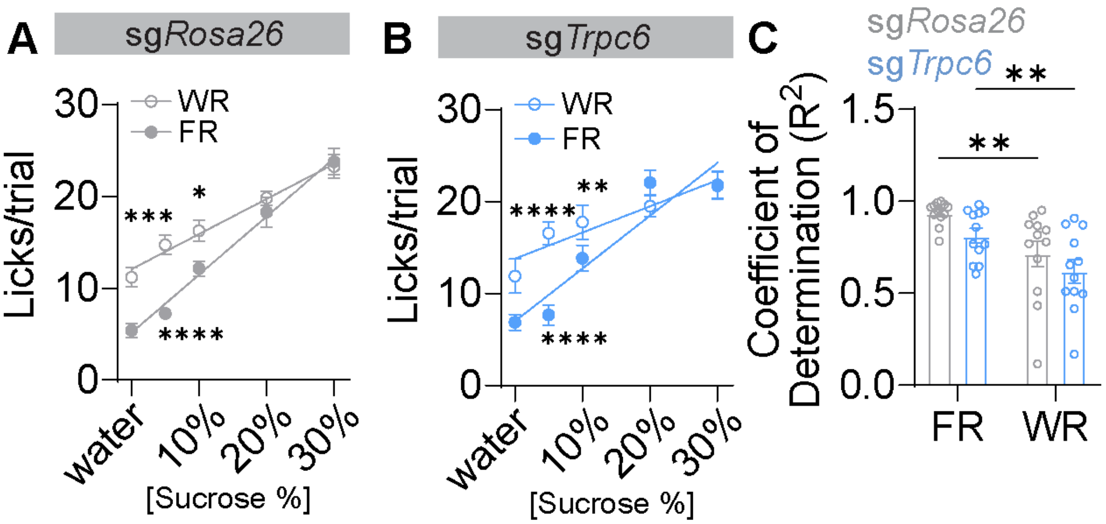

Supplemental Figure 2. Water restriction elicits higher licking responses at lower but not higher sucrose concentrations than food restriction in both sg*Rosa26* and sg*Trpc6* mice. (A-B) Licking responses for water and increasing sucrose in sg*Rosa26* (A) and sg*Trpc6* (B) mice. Two-way repeated measures ANOVA within subject comparison (*P<0.05, **P<0.01, ***P<0.001, and ****P<0.0001, Sidak post hoc comparison). (C) Linear regression analysis for individual mice reveals significant differences within sg*Rosa26* under food restriction (FR) versus water restriction (WR) and within sg*Trpc6* mice under FR versus WR (Two-way repeated measures ANOVA; **P<0.01, ***P<0.001, and ****P<0.0001, Sidak post hoc comparison). Data are presented as mean ± S.E.M.

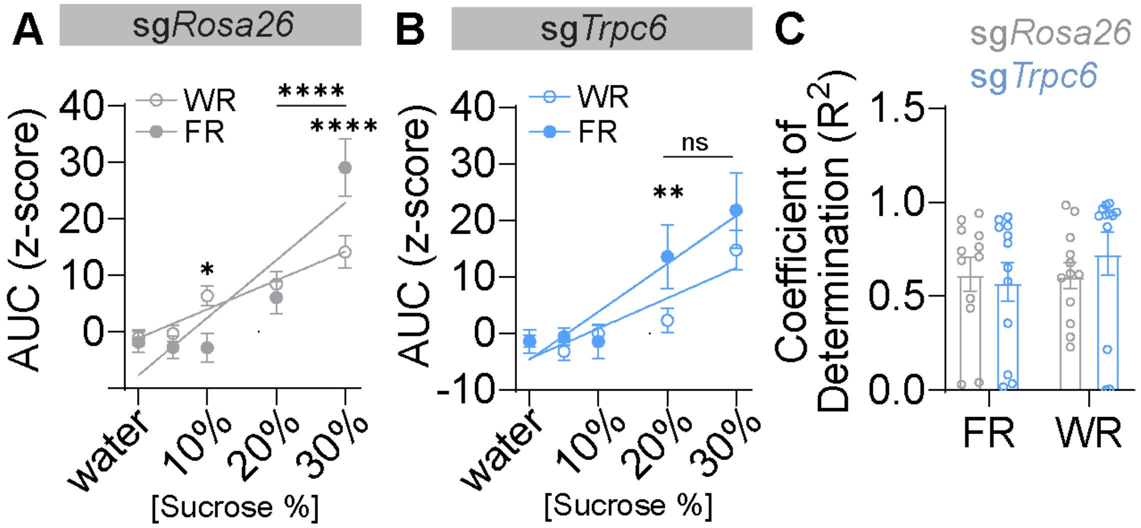

Supplemental Figure 3. Differential calcium responses following the solution access period in sg*Rosa26* and sg*Trpc6* mice. (A-B) GCaMP6m signal AUC of 10s post access period in response to water and increasing sucrose in sg*Rosa26* (A) and sg*Trpc6* (B) mice. In sg*Rosa26* mice (A), there are significantly larger responses to 10% sucrose under WR compared to FR and significantly larger responses to 30% sucrose in FR compared to WR. Like the AUC for the access period, the AUC for the post access period is larger at 30% compared to 20% under FR. In sg*Trpc6* mice (B) there are significantly larger responses to 20% sucrose FR compared to WR. However, unlike sg*Rosa26* mice, there is no significant difference in the AUC for the post access period at 30% compared to 20% under FR. (A-B) Two-way repeated measures ANOVA within subject comparison (*P<0.05, **P<0.01, and ****P<0.0001, Sidak post hoc comparison). (C) Linear regression analysis for individual mice reveals no significant differences between sg*Rosa26* and sg*Trpc6* mice under FR versus WR. Data are presented as mean ± S.E.M.

Extended Data Table 1.

Figure		Test	N	Statistics	P	Posttest	p (post)
			Main Figure Statistics				
1	A	Two-way RM ANOVA	N=7 mice	Interaction: F(6,72)=9.203; Effect of channel type: F(6,72)=15.20; Effect of group: F(1,12)=20.86	P<0.0001, P<0.0001, P=0.0006	Bonferroni multiple comparisons	****p<0.0001
	G	*AUC* D’Agostino & Pearson Test	$N_{sg\mathit{Rosa26}}$=4 mice, $n_{sg\mathit{Rosa26}}$=31 cells; $N_{sg\mathit{Trpc6}}$=3 mice, $n_{sg\mathit{Trpc6}}$=46 cells	$K^2_{sg\mathit{Rosa26}}$=6.614, $K^2_{sg\mathit{Trpc6}}$=13.71	$P_{sg\mathit{Rosa26}}<0.05$, $P_{sg\mathit{Trpc6}}<0.01$		
		AUC Mann—Whitney	$N_{sg\mathit{Rosa26}}$=4 mice, $n_{sg\mathit{Rosa26}}$=31 cells; $N_{sg\mathit{Trpc6}}$=3 mice, $n_{sg\mathit{Trpc6}}$=46 cells	U=412	P<0.01		
		Peak D’Agostino & Pearson Test	$N_{sg\mathit{Rosa26}}$=4 mice, $n_{sg\mathit{Rosa26}}$=31 cells; $N_{sg\mathit{Trpc6}}$=3 mice, $n_{sg\mathit{Trpc6}}$=46 cells	$K^2_{sg\mathit{Rosa26}}$=11.78, $K^2_{sg\mathit{Trpc6}}$=33.68	$P_{sg\mathit{Rosa26}}<0.01$, $P_{sg\mathit{Trpc6}}<0.0001$		
		Peak Mann—Whitney	$N_{sg\mathit{Rosa26}}$=4 mice, $n_{sg\mathit{Rosa26}}$=31 cells; $N_{sg\mathit{Trpc6}}$=3 mice, $n_{sg\mathit{Trpc6}}$=46 cells	U=378	P<0.001		
	H	*Proportion* Chi-square	$Nonresponder_{sg\mathit{Rosa26}}$=4 cells, $Responder_{sg\mathit{Rosa26}}$=27 cells; $Nonresponder_{sg\mathit{Trpc6}}$=21 cells, $Responder_{sg\mathit{Trpc6}}$=25 cells	χ^2=9.059, df=1, N=77	P<0.01		
	J	*AUC* D’Agostino & Pearson Test	$N_{sg\mathit{Rosa26}}$=3 mice, $n_{sg\mathit{Rosa26}}$=36 cells; $N_{sg\mathit{Trpc6}}$=3 mice, $n_{sg\mathit{Trpc6}}$=47 cells	$K^2_{sg\mathit{Rosa26}}$=13.52, $K^2_{sg\mathit{Trpc6}}$=53.47	$P_{sg\mathit{Rosa26}}<0.01$, $P_{sg\mathit{Trpc6}}<0.0001$		
		AUC Mann—Whitney	$N_{sg\mathit{Rosa26}}$=3 mice, $n_{sg\mathit{Rosa26}}$=36 cells; $N_{sg\mathit{Trpc6}}$=3 mice, $n_{sg\mathit{Trpc6}}$=47 cells	U=598	P<0.05		
		Peak D’Agostino & Pearson Test	$N_{sg\mathit{Rosa26}}$=3 mice, $n_{sg\mathit{Rosa26}}$=36 cells; $N_{sg\mathit{Trpc6}}$=3 mice, $n_{sg\mathit{Trpc6}}$=47 cells	$K^2_{sg\mathit{Rosa26}}$=6.847, $K^2_{sg\mathit{Trpc6}}$=55.97	$P_{sg\mathit{Rosa26}}<0.05$, $P_{sg\mathit{Trpc6}}<0.0001$		
		Peak Mann—Whitney	$N_{sg\mathit{Rosa26}}$=3 mice, $n_{sg\mathit{Rosa26}}$=36 cells;	U=523	P<0.01		

			$N_{sg\mathit{Trpc6}}$=3 mice, $n_{sg\mathit{Trpc6}}$=47 cells				
	K	*Proportion* Chi-square	Nonresponder$_{sg\mathit{Rosa26}}$=10 cells, Responder$_{sg\mathit{Rosa26}}$=26 cells; Nonresponder$_{sg\mathit{Trpc6}}$=33 cells, Responder$_{sg\mathit{Trpc6}}$=14 cells	χ^2=14.70, df=1, N=83	P<0.0001		
2	A	*AUC* D'Agostino & Pearson Test	$N_{sg\mathit{Rosa26}}$=4 mice, $n_{sg\mathit{Rosa26}}$=34 cells; $N_{sg\mathit{Trpc6}}$=4 mice, $n_{sg\mathit{Trpc6}}$=33 cells	$K^2_{sg\mathit{Rosa26}}$=12.94, $K^2_{sg\mathit{Trpc6}}$=15.96	$P_{sg\mathit{Rosa26}}$<0.01, $P_{sg\mathit{Trpc6}}$<0.001		
		AUC Mann—Whitney	$N_{sg\mathit{Rosa26}}$=4 mice, $n_{sg\mathit{Rosa26}}$=34 cells; $N_{sg\mathit{Trpc6}}$=4 mice, $n_{sg\mathit{Trpc6}}$=33 cells	U=289	P<0.001		
		Peak D'Agostino & Pearson Test	$N_{sg\mathit{Rosa26}}$=4 mice, $n_{sg\mathit{Rosa26}}$=34 cells; $N_{sg\mathit{Trpc6}}$=4 mice, $n_{sg\mathit{Trpc6}}$=33 cells	$K^2_{sg\mathit{Rosa26}}$=2.610, $K^2_{sg\mathit{Trpc6}}$=3.770	$P_{sg\mathit{Rosa26}}$=ns, $P_{sg\mathit{Trpc6}}$=ns		
		Peak Independent t-test	$N_{sg\mathit{Rosa26}}$=4 mice, $n_{sg\mathit{Rosa26}}$=34 cells; $N_{sg\mathit{Trpc6}}$=4 mice, $n_{sg\mathit{Trpc6}}$=33 cells	t=2.722, df=65	P<0.01		
		Proportion Chi-square	Nonresponder$_{sg\mathit{Rosa26}}$=6 cells, Responder$_{sg\mathit{Rosa26}}$=28 cells; Nonresponder$_{sg\mathit{Trpc6}}$=10 cells, Responder$_{sg\mathit{Trpc6}}$=23 cells	χ^2=1.476, df=1, N=67	P=ns		
	B	Independent t-test	$N_{sg\mathit{Rosa26}}$=3 mice, $n_{sg\mathit{Rosa26}}$=290 cells; $N_{sg\mathit{Trpc6}}$=3 mice, $n_{sg\mathit{Trpc6}}$=512 cells	t=4.959, df=800	P<0.0001		
	C	Independent t-test	$N_{sg\mathit{Rosa26}}$=3 mice, $n_{sg\mathit{Rosa26}}$=10 slices; $N_{sg\mathit{Trpc6}}$=3 mice, $n_{sg\mathit{Trpc6}}$=9 slices	t=3.153, df=17	P<0.01		
	D	*Proportion* Fisher's exact test	Type I$_{sg\mathit{Rosa26}}$=66 cells, Type II$_{sg\mathit{Rosa26}}$=33 cells,		P<0.001		

			Type $III_{sgRosa26}$=1; Type $I_{sgTrpc6}$=89 cells, Type $II_{sgTrpc6}$=10 cells, Type $III_{sgTrpc6}$=1 cells				
	E	*Frequency* D'Agostino & Pearson Test	$N_{sgRosa26}$=3 mice, $n_{sgRosa26}$=84 cells; $N_{sgTrpc6}$=3 mice, $n_{sgTrpc6}$=52 cells	$K^2_{sgRosa26}=14.42$, $K^2_{sgTrpc6}=10.16$	$P_{sgRosa26}<0.001$, $P_{sgTrpc6}<0.01$		
		Frequency Mann—Whitney	$N_{sgRosa26}$=3 mice, $n_{sgRosa26}$=84 cells; $N_{sgTrpc6}$=3 mice, $n_{sgTrpc6}$=52 cells	U=1452	P<0.001		
		AUC D'Agostino & Pearson Test	$N_{sgRosa26}$=3 mice, $n_{sgRosa26}$=84 cells; $N_{sgTrpc6}$=3 mice, $n_{sgTrpc6}$=52 cells	$K^2_{sgRosa26}=28.22$, $K^2_{sgTrpc6}=14.62$	$P_{sgRosa26}<0.0001$, $P_{sgTrpc6}<0.001$		
		AUC Mann—Whitney	$N_{sgRosa26}$=3 mice, $n_{sgRosa26}$=84 cells; $N_{sgTrpc6}$=3 mice, $n_{sgTrpc6}$=52 cells	U=2174	P=ns		
	F	*AUC* D'Agostino & Pearson Test	$N_{sgRosa26}$=3 mice, $n_{sgRosa26}$=40 cells; $N_{sgTrpc6}$=3 mice, $n_{sgTrpc6}$=30 cells	$K^2_{sgRosa26}=33.54$, $K^2_{sgTrpc6}=50.69$	$P_{sgRosa26}<0.0001$, $P_{sgTrpc6}<0.0001$		
		AUC Mann—Whitney	$N_{sgRosa26}$=3 mice, $n_{sgRosa26}$=40 cells; $N_{sgTrpc6}$=3 mice, $n_{sgTrpc6}$=30 cells	U=349	P<0.01		
		Peak D'Agostino & Pearson Test	$N_{sgRosa26}$=3 mice, $n_{sgRosa26}$=40 cells; $N_{sgTrpc6}$=3 mice, $n_{sgTrpc6}$=30 cells	$K^2_{sgRosa26}=6.054$, $K^2_{sgTrpc6}=39.26$	$P_{sgRosa26}<0.05$, $P_{sgTrpc6}<0.0001$		
		Peak Mann—Whitney	$N_{sgRosa26}$=3 mice, $n_{sgRosa26}$=40 cells; $N_{sgTrpc6}$=3 mice, $n_{sgTrpc6}$=30 cells	U=369	P<0.01		
		Proportion Chi-square	$Nonresponder_{sgRosa26}$=11 cells, $Responder_{sgRosa26}$=29 cells; $Nonresponder_{sgTrpc6}$=15 cells, $Responder_{sgTrpc6}$=15 cells	$\chi^2=3.717$, df=1, N=70	P<0.05		

	G	*AUC* D'Agostino & Pearson Test	$N_{sgRosa26}=3$ mice, $n_{sgRosa26}=27$ cells; $N_{sgTrpc6}=3$ mice, $n_{sgTrpc6}=32$ cells	$K^2_{sgRosa26}=29.76$, $K^2_{sgTrpc6}=20.39$	$P_{sgRosa26}<0.0001$, $P_{sgTrpc6}<0.0001$		
		AUC Mann—Whitney	$N_{sgRosa26}=3$ mice, $n_{sgRosa26}=27$ cells; $N_{sgTrpc6}=3$ mice, $n_{sgTrpc6}=32$ cells	U=393	P=ns		
		Peak D'Agostino & Pearson Test	$N_{sgRosa26}=3$ mice, $n_{sgRosa26}=27$ cells; $N_{sgTrpc6}=3$ mice, $n_{sgTrpc6}=32$ cells	$K^2_{sgRosa26}=32.50$, $K^2_{sgTrpc6}=14.76$	$P_{sgRosa26}<0.0001$, $P_{sgTrpc6}<0.001$		
		Peak Mann—Whitney	$N_{sgRosa26}=3$ mice, $n_{sgRosa26}=27$ cells; $N_{sgTrpc6}=3$ mice, $n_{sgTrpc6}=32$ cells	U=398	P=ns		
		Proportion Chi-square	$Nonresponder_{sgRosa26}=4$ cells, $Responder_{sgRosa26}=23$ cells; $Nonresponder_{sgTrpc6}=8$ cells, $Responder_{sgTrpc6}=24$ cells	$\chi^2=0.9376$, df=1, N=59	P=ns		
	H	*AUC* D'Agostino & Pearson Test	$N_{sgRosa26}=3$ mice, $n_{sgRosa26}=20$ cells; $N_{sgTrpc6}=4$ mice, $n_{sgTrpc6}=37$ cells	$K^2_{sgRosa26}=13.89$, $K^2_{sgTrpc6}=46.10$	$P_{sgRosa26}<0.01$, $P_{sgTrpc6}<0.0001$		
		AUC Mann—Whitney	$N_{sgRosa26}=3$ mice, $n_{sgRosa26}=20$ cells; $N_{sgTrpc6}=4$ mice, $n_{sgTrpc6}=37$ cells	U=313	P=ns		
		Peak D'Agostino & Pearson Test	$N_{sgRosa26}=3$ mice, $n_{sgRosa26}=20$ cells; $N_{sgTrpc6}=4$ mice, $n_{sgTrpc6}=37$ cells	$K^2_{sgRosa26}=6.594$, $K^2_{sgTrpc6}=30.73$	$P_{sgRosa26}<0.05$, $P_{sgTrpc6}<0.0001$		
		Peak Mann—Whitney	$N_{sgRosa26}=3$ mice, $n_{sgRosa26}=20$ cells; $N_{sgTrpc6}=4$ mice, $n_{sgTrpc6}=37$ cells	U=251.5	P<0.05		

		Proportion Chi-square	Nonresponder$_{sg\textit{Rosa26}}$=3 cells, Responder$_{sg\textit{Rosa26}}$=17 cells; Nonresponder$_{sg\textit{Trpc6}}$=8 cells, Responder$_{sg\textit{Trpc6}}$=29 cells	χ^2=0.3655, df=1, N=57	P=ns		
3	B	*Proportion* Fisher's exact test	Spontaneous$_{sg\textit{Rosa26}}$=42 cells, Inactive$_{sg\textit{Rosa26}}$=34 cells; Spontaneous$_{sg\textit{Trpc6}}$=39 cells, Inactive$_{sg\textit{Trpc6}}$=27 cells		P=ns		
	C	D'Agostino & Pearson Test	N$_{sg\textit{Rosa26}}$=5 mice, n$_{sg\textit{Rosa26}}$=65 cells; N$_{sg\textit{Trpc6}}$=6 mice, n$_{sg\textit{Trpc6}}$=80 cells	$K^2_{sg\textit{Rosa26}}$=42.53, $K^2_{sg\textit{Trpc6}}$=39.38	P $_{sg\textit{Rosa26}}$<0.0001, P $_{sg\textit{Trpc6}}$<0.0001		
		Mann—Whitney	N$_{sg\textit{Rosa26}}$=5 mice, n$_{sg\textit{Rosa26}}$=65 cells; N$_{sg\textit{Trpc6}}$=6 mice, n$_{sg\textit{Trpc6}}$=80 cells	U=2445	P=ns		
	D	D'Agostino & Pearson Test	N$_{sg\textit{Rosa26}}$=5 mice, n$_{sg\textit{Rosa26}}$=51 cells; N$_{sg\textit{Trpc6}}$=6 mice, n$_{sg\textit{Trpc6}}$=56 cells	$K^2_{sg\textit{Rosa26}}$=46.31, $K^2_{sg\textit{Trpc6}}$=85.21	P $_{sg\textit{Rosa26}}$<0.0001, P $_{sg\textit{Trpc6}}$<0.0001		
		Mann—Whitney	N$_{sg\textit{Rosa26}}$=5 mice, n$_{sg\textit{Rosa26}}$=51 cells; N$_{sg\textit{Trpc6}}$=6 mice, n$_{sg\textit{Trpc6}}$=56 cells	U=1377	P=ns		
	E	D'Agostino & Pearson Test	N$_{sg\textit{Rosa26}}$=5 mice, n$_{sg\textit{Rosa26}}$=65 cells; N$_{sg\textit{Trpc6}}$=6 mice, n$_{sg\textit{Trpc6}}$=67 cells	$K^2_{sg\textit{Rosa26}}$=7.325, $K^2_{sg\textit{Trpc6}}$=6.143	P $_{sg\textit{Rosa26}}$<0.05, P $_{sg\textit{Trpc6}}$<0.05		
		Mann—Whitney	N$_{sg\textit{Rosa26}}$=5 mice, n$_{sg\textit{Rosa26}}$=65 cells; N$_{sg\textit{Trpc6}}$=6 mice, n$_{sg\textit{Trpc6}}$=67 cells	U=2134	P=ns		
	F	D'Agostino & Pearson Test	N$_{sg\textit{Rosa26}}$=8 mice, n$_{sg\textit{Rosa26}}$=28 cells; N$_{sg\textit{Trpc6}}$=3 mice, n$_{sg\textit{Trpc6}}$=36 cells	$K^2_{sg\textit{Rosa26}}$=10.16, $K^2_{sg\textit{Trpc6}}$=1.330	P $_{sg\textit{Rosa26}}$<0.01, P $_{sg\textit{Trpc6}}$=ns		

		Mann—Whitney	$N_{sg\mathit{Rosa26}}$=8 mice, $n_{sg\mathit{Rosa26}}$=28 cells; $N_{sg\mathit{Trpc6}}$=3 mice, $n_{sg\mathit{Trpc6}}$=36 cells	U=473	P=ns		
	H	Two-way RM ANOVA	$N_{sg\mathit{Rosa26}}$=13 mice, $n_{sg\mathit{Rosa26}}$=15 cells; $N_{sg\mathit{Trpc6}}$=9 mice, $n_{sg\mathit{Trpc6}}$=26 cells	Effect of step: F(1.893, 73.83); Effect of subject: F(39, 897) = 49.89	Effect of step: P<0.0001; Effect of subject: P<0.0001	Bonferroni's multiple comparisons	p=ns
4	D	Two-way RM ANOVA	$N_{sg\mathit{Rosa26}}$=12 mice, $N_{sg\mathit{Trpc6}}$=12 mice	Effect of spout ID: F(4,88) = 43.02; Effect of subject: F(22,88) = 7.247	Effect of spout ID: P<0.0001; Effect of subject: P<0.0001	Tukey's multiple comparisons	*p<0.05, **p<0.01, ***p<0.001, ****p<0.0001
	E	Independent t-test	$N_{sg\mathit{Rosa26}}$=12 mice, $N_{sg\mathit{Trpc6}}$=12 mice	t=0.9955, df=22	P=ns		
	G	Two-way RM ANOVA	$N_{sg\mathit{Rosa26}}$=12 mice, $N_{sg\mathit{Trpc6}}$=12 mice	Interaction: F(4,88) = 3.413; Effect of spout ID: F(4,88) = 174.2; Effect of subject: F(22,88) = 7.311	Interaction: P=0.0121 Effect of spout ID: P<0.0001; Effect of subject: P<0.0001	Tukey's multiple comparisons	*p<0.05, **p<0.01, ***p<0.001, ****p<0.0001
	H	Independent t-test	$N_{sg\mathit{Rosa26}}$=12 mice, $N_{sg\mathit{Trpc6}}$=12 mice	t=2.823, df=22	P<0.01		
5	B	Two-way RM ANOVA	$N_{sg\mathit{Rosa26}}$=12 mice, $N_{sg\mathit{Trpc6}}$=12 mice	Effect of spout ID: F(4,88) = 41.87; Effect of subject: F(22,88) = 4.052	Effect of spout ID: P<0.0001; Effect of subject: P<0.0001	Tukey's multiple comparisons	*p<0.05, **p<0.01, ***p<0.001, ****p<0.0001
	C	Independent t-test	$N_{sg\mathit{Rosa26}}$=12 mice, $N_{sg\mathit{Trpc6}}$=12 mice	t=0.8182, df=22	P=ns		

	E	Two-way RM ANOVA	$N_{sg\mathit{Rosa26}}$=12 mice, $N_{sg\mathit{Trpc6}}$=12 mice	Effect of spout ID: F(4,88) = 49.11; Effect of subject: F(22,88) = 3.362	Effect of spout ID: P<0.0001; Effect of subject: P<0.0001	Tukey's multiple comparisons	*p=0.0505, **p<0.01, ***p<0.001, ****p<0.0001
	F	Independent t-test	$N_{sg\mathit{Rosa26}}$=12 mice, $N_{sg\mathit{Trpc6}}$=12 mice	t=1.284, df=22	P=ns		
	G	*Water* Paired t-test	N_{WR}=12 mice; N_{FR}=12 mice	t = 3.647, df = 11	P<0.01		
		5% sucrose Paired t-test	N_{WR}=12 mice; N_{FR}=12 mice	t = 5.608, df = 11	P<0.001		
		10% sucrose Paired t-test	N_{WR}=12 mice; N_{FR}=12 mice	t = 4.546, df = 11	P<0.001		
		20% sucrose Paired t-test	N_{WR}=12 mice; N_{FR}=12 mice	t = 0.6625, df = 11	P=ns		
		30% sucrose Paired t-test	N_{WR}=12 mice; N_{FR}=12 mice	t = 2.439, df = 11	P<0.05		
	H	*Water* Paired t-test	N_{WR}=12 mice; N_{FR}=12 mice	t = 0.5427, df = 11	P=ns		
		5% sucrose Paired t-test	N_{WR}=12 mice; N_{FR}=12 mice	t = 2.206, df = 11	P<0.05		

		10% sucrose Paired t-test	N_{WR}=12 mice; N_{FR}=12 mice	t = 1.955, df = 11	P=ns		
		20% sucrose Paired t-test	N_{WR}=12 mice; N_{FR}=12 mice	t = 1.681, df = 11	P=ns		
		30% sucrose Paired t-test	N_{WR}=12 mice; N_{FR}=12 mice	t = 0.01657, df = 11	P=ns		
Supplementary Data Statistics						
1	D	Independent t-test	$N_{sgRosa26}$=12 mice, $N_{sgTrpc6}$=12 mice	t=1.113, df=22	P=ns		
2	A	sg*Rosa26* Two-way RM ANOVA, within group comparisons	N_{WR}=12 mice; N_{FR}=12 mice	Interaction: F(4, 44)=6.388; Effect of spout ID: F(4, 44) = 96.08; Effect of restriction: F(1, 11)=24.25	Interaction: P=0.0004; Effect of spout ID: P<0.0001; Effect of restriction: P=0.0005	Sidak's multiple comparisons	*p<0.05, **p<0.01, ***p<0.001, ****p<0.0001
	B	sg*Trpc6* Two-way RM ANOVA, within group comparisons	N_{WR}=12 mice; N_{FR}=12 mice	Interaction: F(4, 44)=19.65; Effect of spout ID: F(4, 44) = 75.86	Interaction: P<0.0001; Effect of spout ID: P<0.0001	Sidak's multiple comparisons	*p<0.05, **p<0.01, ***p<0.001, ****p<0.0001
	C	*Regression Coefficient* Two-way RM ANOVA	$N_{sgRosa26}$=12 mice, $N_{sgTrpc6}$=12 mice	Effect of restriction: F(1,22) = 21.36	P=0.0001	Uncorrected Fisher's LSD	**p<0.01
3	A	sg*Rosa26* Two-way RM ANOVA, within group comparisons	N_{WR}=12 mice; N_{FR}=12 mice	Interaction: F(4, 44)=9.717; Effect of spout ID: F(4, 44) = 23.36	Interaction: P<0.0001; Effect of spout ID: P<0.0001	Sidak's multiple comparisons	*p<0.05, **p<0.01, ***p<0.001, ****p<0.0001

	B	sg*Trpc6* Two-way RM ANOVA, within group comparisons	N_{WR}=12 mice; N_{FR}=12 mice	Interaction: F(4, 44)=3.110; Effect of spout ID: F(4, 44) = 12.77	Interaction: P=0.0244; Effect of spout ID: P<0.0001	Sidak's multiple comparisons	*p<0.05, **p<0.01, ***p<0.001, ****p<0.0001
	C	*Regression Coefficient* Two-way RM ANOVA	$N_{sgRosa26}$=12 mice, $N_{sgTrpc6}$=12 mice		P=ns	Sidak's multiple comparisons	P=ns

CHAPTER 3: OTHER TRPC6 CHANNEL INVESTIGATIONS

3.1 Trpc6 in situ hybridization experiment

Although the FACS data for our sg*Trpc6*(1) and sg*Trpc*(2) CRISPR viruses confirmed ~70-80% mutagenesis efficiency (Fig. 1D, E – pie charts), we also wanted to confirm a reduction in *Trpc6* mRNA. I bilaterally injected AAV1-FLEX-sg*Rosa26* (control group) or AAV1-FLEX-sg*Trpc6*(1) and AAV1-FLEX-sg*Trpc*(2) (experimental group) into the VTA of DAT-Cre mice. Four weeks later, Sage Cho, a post baccalaureate student in the lab, performed *in situ* hybridization (ISH) with probes for *Trpc6* and *Th.* After several rounds of ISH across two cohorts of mice, we saw a modest, but significant, reduction in *Trpc6* mRNA in the experimental group (Fig. 6B). However, we expected this reduction to be greater based on previous ISH CRISPR validation experiments that have been performed in the lab. Some experimental slices had a very visible reduction in *Trpc6* mRNA (Fig. 6A), but some slices appeared to have no reduction.

To confirm that all slices had CRISPR virus expression, Sage performed another round of ISH with probes for *Th* and *Cas9*. We saw abundant *Cas9* expression, confirming that the virus had been injected in the VTA. Thus, it was strange that we only saw a ~30% reduction in *Trpc6* mRNA (Fig. 6B); we focused our work on other experiments for the time being.

Additionally, we wanted to confirm that there was no overcompensation of other TRPC channels after the mutagenesis of *Trpc6*. In a different cohort of mice, I bilaterally injected AAV1-FLEX-sg*Rosa26* (control group) or AAV1-FLEX-sg*Trpc6*(1) and AAV1-FLEX-sg*Trpc*(2) (experimental group) into the VTA of DAT-Cre mice. Four weeks later, Sage performed one round of hybridization chain reaction (HCR) with a probe for *Th,* imaged the sections, stripped the probe, and then performed one round of ISH with probes for *Trpc3, Trpc4,* and *Trpc6.* We chose *Trpc3* because TRPC3 channels are in the same subfamily as TRPC6 and can form heteromers with

TRPC6. We chose *Trpc4* because it has the second highest enrichment (after *Trpc6*) in VTA-DA neurons compared to non DA cells (Fig. iA).

Due to multiple technical issues such as unusually high background fluorescence, slice degradation, and misaligned tiling, it was difficult to quantify the signal using automated software (QuPath). Both Sage and I independently tried to analyze the data using QuPath, but did not get meaningful results. Furthermore, we did not see a reduction in *Trpc6* mRNA in the experimental group that would confirm our findings from our first ISH experiment (Fig. 6), which made these results even more suspicious. Either there was a technical problem during the HCR/ISH process or the probes weren't working as expected. Taken together with our initial (very modest) reduction in *Trpc6* mRNA (Fig. 6), we were not able to conclusively demonstrate that there was a reduction in *Trpc6* mRNA after injection of the sg*Trpc6* CRISPR viruses.

However, ISH as a measurement of mRNA knockdown via CRISPR/Cas9 also has caveats. CRISPR/Cas9 technology causes gene knockdown by creating indel mutations at the targeted cut site, which most commonly result in premature termination codons (PTCs). These PTCs lead to the termination of protein synthesis, resulting in truncated and often non-functional proteins that are degraded during translation (Brogna & Wen, 2009). The presence of PTCs is detected by the RNA exon junction complex that canonically senses PTCs associated with aberrant splicing, mistranslation, or mutation to facilitate the de-capping or de-polyadenylation of mRNA promoting decay (Brogna & Wen, 2009). Although this mechanism provides a readout for indels associated CRISPR mutagenesis, there is a high degree of variability amongst transcripts that are sensitive to nonsense mediated decay (NMD), as well as other determinants such as the proximity of the mutation to the start codon and exon-exon junctions (Sato & Singer, 2021). Additional considerations include the rate of NMD and the ability of the probe used during ISH to still bind to mRNA sequences that are downstream or upstream of the CRISPR cut site. Given the general long length of *in situ* probes, the probe may still bind even if there is a point mutation or an in-frame indel (multiples of 3 base pairs) that can produce altered proteins without degrading mRNA. Therefore, in some cases, ISH may underestimate the amount of NMD due to CRISPR/Cas9 mutagenesis. Although our ISH data is inconclusive, we are still confident that our CRISPR/Cas9 mutagenesis strategy is causing a loss TRPC6 channel function based on our FACS data showing ~80% mutagenesis and our functional assay using calcium imaging with the TRPC6 channel direct agonist showing a significant loss of TRPC6 channel function after *Trpc6* mutagenesis (Fig. 1).

3.2 Tacr3-expressing subpopulation

Based on the extensive evidence presented in 1.5 linking TRPC5 channels to the Tacr3 signaling pathway in hypothalamic neurons, I initially started my TRPC6 channel investigation focusing on the *Tacr3* subpopulation of VTA-DA neurons. *Tacr3*-expressing VTA neurons represent a subpopulation of DA neurons that project to both regions of the nucleus accumbens (NAc) and comprise approximately one-third of the DA population in this region (Heymann et al., 2020). Although these cells represent a subset of VTA-DA neurons, mice will perform intracranial optical self-stimulation of specifically VTA-*Tacr3* cell bodies significantly more than controls and exhibit a real-time place preference for VTA-*Tacr3* stimulation (Heymann et al., 2020). This effect is not observed in larger DA subpopulations that project more exclusively to the NAc core and shell, respectively (Heymann et al., 2020). Thus, VTA-*Tacr3* neurons appear to represent a minimally sufficient population of DA neurons that promote reward reinforcement behavior.

To selectively target *Tacr3*-expressing cells, I injected AAV1-FLEX-sg*Rosa26* (control group) or AAV1-FLEX-sg*Trpc6*(1) (experimental group) and Cre-dependent GCaMP6m (both groups) into the VTA of *Tacr3*-Cre mice. The OHRBETS system was not implemented in our lab at the time so I used an operant box to assess reward reinforcement behavior. Food restricted mice were trained on a fixed-ratio 1 (FR1) schedule of reinforcement to press a level for a three second cue, followed by delivery of a 20-mg sucrose pellet. After five days of acquisition of the task, the lever pressing behavior was extinguished over five days and then reinstated for one day. Both groups acquired the task equally and I did not observe any significant differences in learning or calcium signals.

Differences started to emerge however during the reward omission task. During this task, mice were retrained on an FR1 to press an active lever for a sucrose pellet. After mice had sufficiently learned the task, 25%, 50%, or 75% of rewards were omitted during subsequent test sessions (Fig. 7). While the number of lever presses did not differ between groups, sg*Trpc6* mice showed significantly reduced calcium signals compared to controls when a reward was highly unexpected during 75% reward omission (Fig. 7C). Because the majority of *Tacr3* neurons are dopaminergic, these results suggested that mice lacking TRPC6 channels in VTA-*Tacr3* neurons exhibited less DA neuron excitation to a highly unexpected reward. It is well-established that DA signaling encodes the value of reward-predictive stimuli and influences both learning and decision-making (Wise, 2004). Thus, based on these data, I hypothesized that TRPC6 channels may play a role in regulating VTA-*Tacr3* calcium signals during reward uncertainty.

To further investigate the role of TRPC6 channels in reward uncertainty, I recorded the calcium dynamics of VTA-*Tacr3* neurons with and without TRPC6 channels during a probabilistic discounting task (Parker et al., 2011). Probabilistic discounting is the observation that an uncertain reward is generally considered to be worth less compared to the same reward available for certain (Shead & Hodgkins, 2009). The probabilistic discounting task gives mice the ability to choose between a small, certain reward and a large, uncertain reward. This task tested value discrimination in the context of uncertainty and also assessed risk preference behavior.

Parker et al. (2011) reported that control mice choose the high-reward lever 85% of the time when it is reinforced in 100% of trials. As the probability of reinforcement for the high-reward lever decreases to 25%, control mice switch preferences to the low-reward lever because they prefer a smaller but certain reward over a larger unexpected reward (Parker et al., 2011). Because my preliminary operant data indicated that sg*Trpc6* mice have reduced calcium activity for unexpected rewards and potentially a reduced capability to scale their DA signals in general, I hypothesized that sg*Trpc6* mice would exhibit an impaired ability to develop a preference for the high-reward lever and/or a delayed switch from the high-reward lever to the low-reward lever during probabilistic discounting.

Mice completed a modified version of the probabilistic discounting task as described by Parker et al. (2011). A flashing house light signaled the beginning of each trial. Once the mouse made a nose poke into the food receptacle, one of two levers was extended in the chamber. Each lever press was reinforced on an FR1 schedule of reinforcement with a sucrose pellet and followed by a 10s intertrial interval (ITI). The ITI was progressively extended to 60s and the time limit for initiating a trial and executing the lever press was reduced to 20s. Failure to initiate or failure to press the lever in 20s resulted in a missed trial and a 60s timeout. Once animals successfully completed 20 or more of the 24 trials, one lever was randomly assigned to deliver two sucrose pellets (high-reward) and one lever to continue delivering a single sucrose pellet (low-reward). Mice received two training sessions per day: The morning session consisted of 24 forced trials (12 high-reward and 12 low-reward lever presentations) where only one lever was presented. The afternoon session consisted of 24 choice trials where both levers were presented. Once the mice established a preference for the high-reward lever, the probability of reinforcement for the high-reward lever varied across days. The probability of reinforcement was the same in the forced trial and choice trial sessions on a given day so that the mouse experienced the contingencies of each lever in the first session and then decided which lever to press in the second session based on experience.

The major hurdle I encountered when performing the probabilistic discounting task was the amount of time that it took to train the animals on the task. Due to the task structure, mice had to complete a trial in a short amount of time or else they faced a timeout period, which happened often. The frequent timeout periods confused the mice, and thus their learning rate suffered. Mice could only move onto the next phase of the task if they could complete trials with 80% accuracy, which meant that it took them multiple months to complete the entirety of the probabilistic discounting task. After I ran the first cohort of mice, I observed a trend towards impaired discrimination for the high- vs. low- reward levers in the sg*Trpc6* group. However, I repeated the experiment in a second cohort of mice and the effect disappeared.

One of the reasons why I did not observe significant results with mutagenesis of *Trpc6* in *Tacr3*-expressing cells may be because of a small population of *Tacr3*-expressing cells that does not express DA and thus have very little to no TRPC6 channels. Thus, injection of the sg*Trpc6* CRISPR viruses would have no effect on these cells but they would still express GCaMP6m. This means that this population would be included in both the sg*Rosa26* and sg*Trpc6* groups, potentially occluding a subtle yet significant difference in calcium signaling between groups. In retrospect, considering the senktide bath calcium imaging experiment (Chapter 2, Fig. 2E) showing no significant differences in AUC between the sg*Rosa26* and sg*Trpc6* groups and the fact that fiber photometry is a measure of bulk population activity, including this *Tacr3* non-DA population could be the reason why I wasn't seeing significant results.

Single cell RNA-sequencing data from Simon et al. (2024) (that was published after I completed these experiments) confirms that this non-dopaminergic *Tacr3* population is nonzero (Fig. 8), likely reflecting *Tacr3* expression in the underlying interpeduncular nucleus (Lein et al., 2007). The lab has also previously reported that ~15% of neurons virally labeled in the VTA of *Tacr3-Cre* mice are not *Th*-positive (Heymann et al., 2020). Thus, the contribution of non-dopaminergic *Tacr3*- expressing neurons to fiber photometry signals cannot be discounted.

After many months of struggling with the probabilistic discounting task, I changed experimental strategies. Based on the *Tacr3* evidence I gathered, we decided it would be best to expand the scope of the TRPC6 channel project to the entire VTA-DA population instead of only the *Tacr3* subpopulation. For all the experiments I performed onwards, I used DAT-Cre mice instead of *Tacr3*-Cre mice. This pivot ultimately ended generating significant and interesting results as outlined in Chapter 2.

3.3 Figures and legends for Chapter 3

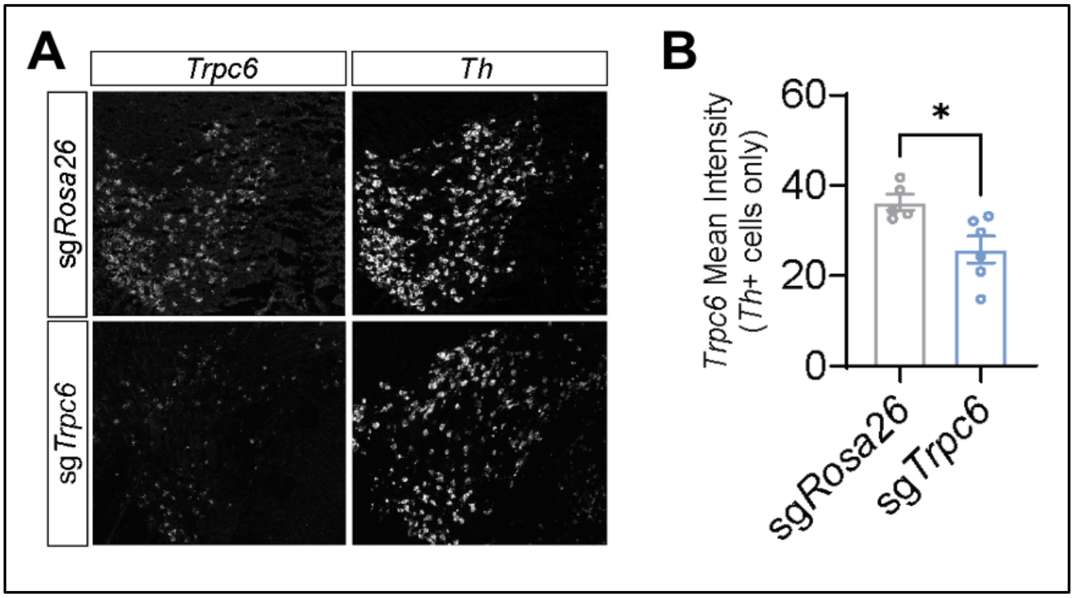

Figure 6. *Trpc6 in situ* hybridization experiment. (A) Example images from sg*Rosa26* (control) and sg*Trpc6* (experimental) slices with probes for *Trpc6* and *Th.* (B) Quantification of *Trpc6* mean intensity in *Th*+ cells only (N=5 mice (sg*Rosa26*); N=6 mice (sg*Trpc6*); Independent t-test, P<0.05).

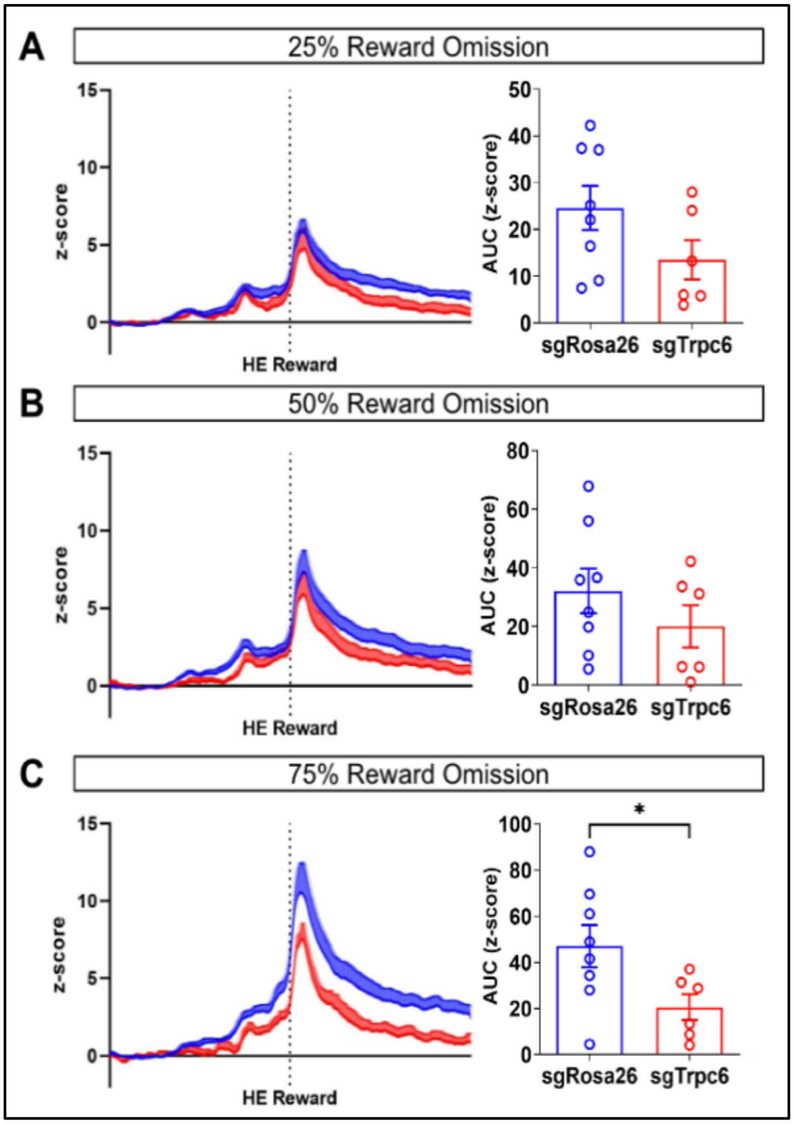

Figure 7. TRPC6 channels contribute to reward encoding during a reward omission task in a subpopulation of DA neurons. Average z-score (+SEM) of the z-scored fiber photometry signals from *Tacr3*-Cre mice aligned to the first head entry (HE) into the food hopper following reward delivery during 25% (A), 50% (B), and 75% (C) reward omission (left). Area under the curve (AUC) of the z-score for the 10 seconds following HE (right) (N=8 sg*Rosa26* mice; N=6 sg*Trpc6* mice; Independent t-test, P<0.05).

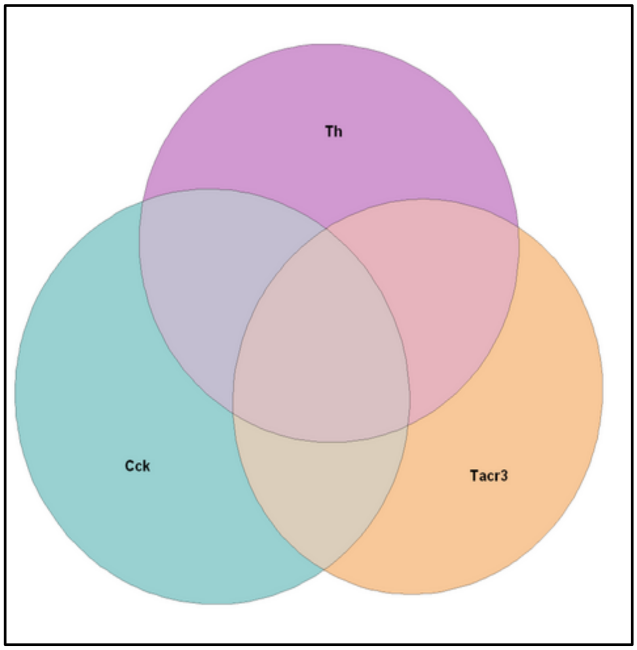

Figure 8. Single cell RNA-sequencing data adapted from Simon et al. (2024). There is a population of *Tacr3*-expressing cells that is non-dopaminergic (the non-overlapping yellow portion).

CHAPTER 4: OTHER PROJECTS

4.1 Spout Mouse hardware construction

The original Zweifel lab OHRBETS design consisted of a single apparatus such that only one mouse could be run at a time (Fig. 9A). Additionally, we were using the NAPE Center's fiber photometry cart to record photometry signals. Each time I wanted to record fiber photometry data, I would have to reserve the cart, collect it from the 1st floor J-wing, transport it across the building to the 6th floor C-wing, record, and then return it back when I was finished. This arrangement was less than ideal for numerous reasons:

1. Running one mouse at a time greatly limited the number of mice per cohort.
2. The OHRBETS system was not built in a sturdy manner - connections would become loose or come apart mid-session.
3. The system consisted of many wires that were unsecured, unlabeled and unorganized, which made debugging issues practically impossible or very time consuming.
4. The NAPE cart was heavily used by other labs so I had to plan out my experiments in advance, but no more than one month in advance.
5. I was limited to six half day NAPE cart reservations every two weeks.
6. Transporting the cart back and forth was cumbersome and detrimental for the health of the equipment, as it was always rattling around during transport.

For these reasons, we decided the Zweifel/Soden labs needed an upgraded OHRBETS system.

I took on the daunting task of building new multi-spout apparatuses. While Dr. Gordon-Fennell had written extremely detailed instructions on how to build the OHRBETS system, I had no experience in 3D printing, soldering or electrical engineering. However, with the help of Mary Loveless (Zweifel/Soden lab research technician) and Dr. Seung-Woo Jin (Zweifel lab post-doc with electrical engineering experience), I was able to successfully build four new multi-spout apparatuses and integrate them with our own new fiber photometry cart (Fig. 9B-D). By the end of this multi-month process, I could run sixteen animals in one cohort (versus six previously) and did not have to rely on the NAPE fiber photometry cart.

4.2 Spout Mouse Python Package

When I first started gathering data from the OHRBETS system, I was using Python scripts that had been written by Joshua Yee (Zweifel/Soden labs research technician) in combination with a GUI written many years ago by Dr. Scott Ng-Evans. Unfortunately, I could not change the way the GUI preprocessed and extracted the signal because the code was "running under the hood" and the Python scripts calculated only surface level parameters. Thus began my journey into the world of coding. Learning how to code also fulfilled a goal of mine which was to fully understand the analysis scripts I had been using to process fiber photometry data instead of blindly running scripts written by other people without knowing what they were doing.

Who better to ask for help than my husband, Daniel McAuley, whose job it is to analyze large data sets for a living? Because I had two different formats of data being stored – data from the Arduino that stored licking behavior and data from the photometry cart that stored calcium signals – integrating the datasets was challenging. One of the main hurdles was that while the lick data stored data about which spout was presented, the fiber photometry data did not have any spout information. Thus, I needed to combine the two datasets in parallel to make sure that correct spout identities were mapped to the photometry signals. Dr. Gordon-Fennell had written R scripts for his paper, but I wanted to learn Python, and therefore Daniel and I decided it would be best if I wrote the scripts from scratch.

Daniel taught me about efficient data storage, organization, and best coding practices. With his (and ChatGPT's) help, I was able to combine the datasets in an organized way, with variables and functions that allowed the user to change analysis parameters depending on his/her needs. At the time, the lab had ongoing discussions about the correct way to process and z-score the photometry signals, and the way we were doing these processes was constantly changing. The code that I wrote allowed the user to make changes, which was something that the previous GUI did not allow, to the preprocessing and z-scoring steps depending on the experimental parameters and/or preferences of the user. In this way, if the user decided he/she wanted to tweak an analysis parameter, he/she could easily rerun the code and reprocess all data from all cohorts at the same time.

Another key feature of the code is the Google Sheets integration. Google Sheets stored the experimental metadata: name of the experiment, cohort number, spout identity (Fig. 10A). One cohort of mice that completed the multi-sucrose experiment was assigned five spout identities across five days. Additionally, the spout identities changed every day and across cohorts. Thus, it was critical that the correct spout identity was mapped to the corresponding lick data and photometry data. In the "old" scripts, the user would manually type in the spout identity (e.g. spout 1: water, spout 2: 5% sucrose, spout 3: 10% sucrose, etc.). Not only was this an error prone and tedious way to assign spout identities, but also didn't allow for processing of multiple days of data at the same time (because there was nowhere to specify *cohort* and *day,* and each cohort and day had different spout assignments). Google Sheets integration solved this problem because the user would specify the experiment name, cohort, and day, and the code would automatically pull the corresponding spout identities from the Google sheet (Fig. 10B).

Daniel and I also put my analysis scripts into a Python package that is published on GitHub (Fig. 11), which streamlined the amount of code that I ran daily and was an introduction to software development. Additionally, I held a coding workshop for the lab to share all that I had learned in this process. While programming was not something I envisioned myself doing prior to starting graduate school, I am very happy that I was able to not only write my own analysis scripts, but also help others with their scripts as well.

4.3 Other collaborations

4.3.1 Lateral septum Pdyn-expressing cells are inhibited during reward retrieval

I took part in a collaboration with a postdoctoral fellow, Dr. Travis Goode, in the Sahay lab at the Center for Regenerative Medicine at Massachusetts General Hospital investigating the role of prodynorphin (*Pdyn*)-expressing inhibitory neurons of the dorsal lateral septum (DLS) in contextual feeding. Using optogenetics and food consumption behavior tasks, Dr. Goode had already shown that optogenetic activation of DLS-*Pdyn* cells reduces feeding and increases avoidance. He now wanted to use fiber photometry to record DLS-*Pdyn* cells in different contexts during consumption. Because the Sahay lab did not have fiber photometry capability, Dr. Goode came to UW for these experiments.

I helped him strategize coordinates for GCaMP injections and optic fiber implantations, showed him how to do the surgeries, discussed experimental design, taught him how to run fiber photometry experiments in our operant boxes, and performed histological validation. We injected a Cre-dependent GCaMP6m virus into the DLS of *Pdyn*-Cre mice and implanted an optic fiber over these cells (Fig. 12A-B). During the operant behavior task (Fig. 12C), we found a consistent decrease in activity in DLS-*Pdyn* cells as animals made head entries to consume food that was attenuated in a novel context (Fig. 12F). We also observed an increase in calcium fluorescence that preceded the active lever press, as well as during the conditioned stimulus (Fig. 12F, H). These increases disappeared when animals experienced a context change, highlighting the anticipatory and contextual signals encoded by DLS-*Pdyn* cells. This fiber photometry experiment strengthened the main findings in his paper, which is currently under revision at *Neuron* (Goode et al., 2025).

4.3.2 The manganese transporter SLC30a10 is necessary for dopamine release in the striatum during stimulation of dopamine cell bodies in the SNc

Collaborators at the University of Texas at Austin were investigating the mechanisms of manganese (Mn)-induced motor disease. They generated a mouse strain with knockout of the Mn efflux transporter *Slc30a10* in dopaminergic neurons by crossing a *Slc30a10* flox/flox mouse with a *Th*-Cre mouse. This genetic strategy ensured that *Slc30a10* was only knocked out in dopamine cells (i.e. cells expressing *Th*). While this mouse strain exhibited motor deficits, *in vivo* microdialysis of dopamine release in the striatum revealed no differences between the knockouts and control mice. To further investigate the cause of the motor deficits, I performed an *in vivo* optogenetics experiment for them.

In contrast to the *in vivo* microdialysis experiment where dopamine release was triggered at dopamine neuron terminals in the dorsal striatum, in the optogenetics experiment, dopamine release in the dorsal striatum was evoked by optogenetically stimulating dopaminergic cell bodies in the substantia nigra pars compacta (SNc). I injected an AAV containing a Cre-dependent expression cassette for the red light-sensitive ion channel, Chrimson (AAV1-CAG-FLEX-Chrimson-tdTomato) into the SNc and an AAV containing the non-conditional expression cassette for the dopamine sensor GRAB-DA (AAV1-hSyn-GRAB-gDA3m) into the dorsal striatum of experimental mice (*Slc30a10* fl/fl:: *Th*-Cre) and what I thought were control mice (i.e. mice that did not have the *Slc30a10* knock out) (Fig. 13a). In reality, the collaborators had misunderstood the experimental parameters and had sent us Cre-negative mice as controls because this was the control group they used in their other experiments. Because the Chrimson virus was Cre-dependent, it was not expressed in Cre-negative mice. Therefore, I redid the experiment in a new cohort with the proper control mice (*Th*-Cre mice). Lesson learned: triple check the experimental parameters with collaborators who are not familiar with the type of experiment that is being performed.

Optogenetic stimulation of SNc cell bodies evoked dopamine release in the dorsal striatum that increased with stimulus duration and stimulation frequency in control mice, but that was not observed in dopaminergic-specific *Slc30a10* knockout mice (Fig. 13c-f). Thus, the microdialysis and optogenetics assays implied that striatal dopamine release in dopaminergic-specific *Slc30a10* knockouts is significantly compromised when dopamine release is evoked through cell body stimulation but not through direct terminal stimulation. Taken together with the rest of the work by the Mukhopadhyay lab, these results suggest that a deficit in evoked dopamine release through cell body stimulation may explain the underlying motor phenotype in *Slc30a10* knockout mice. This work resulted in co-authorship of a manuscript that is under review at *PNAS* (Grant et al., 2025).

4.4 Figures and legends for Chapter 4

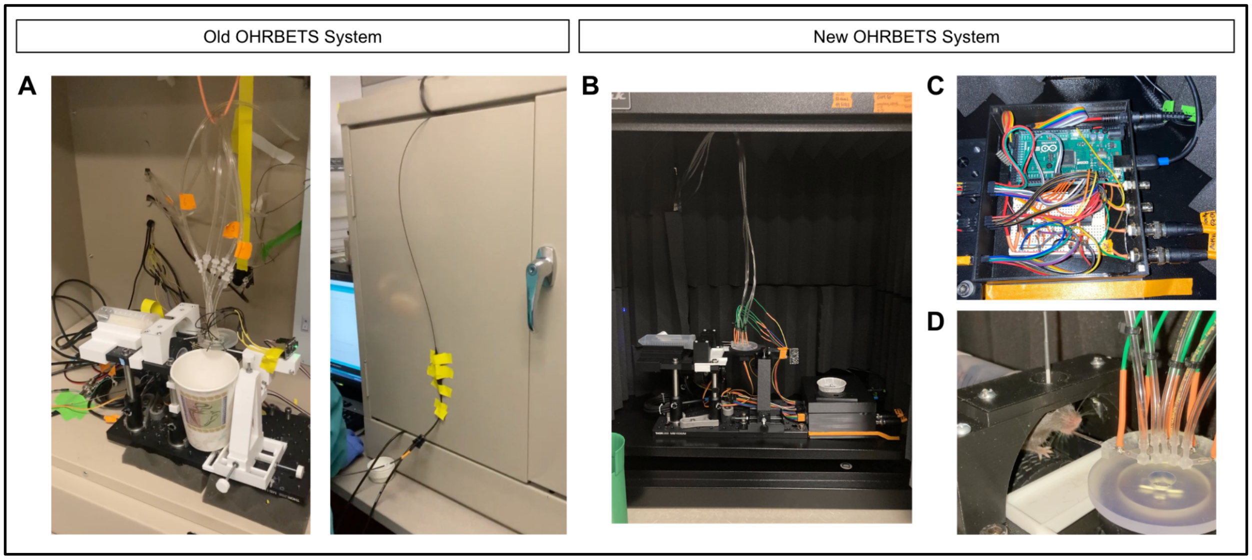

Figure 9. Upgraded Zweifel/Soden labs OHRBETS system. (A) The old set up only allowed one mouse to be run at a time. (B) One (out of four) new apparatuses. (C) Organized and labeled cables. (D) A mouse completing an operant behavior task. A quarter turn of the wheel results in spout extension and delivery of a 10% sucrose solution.

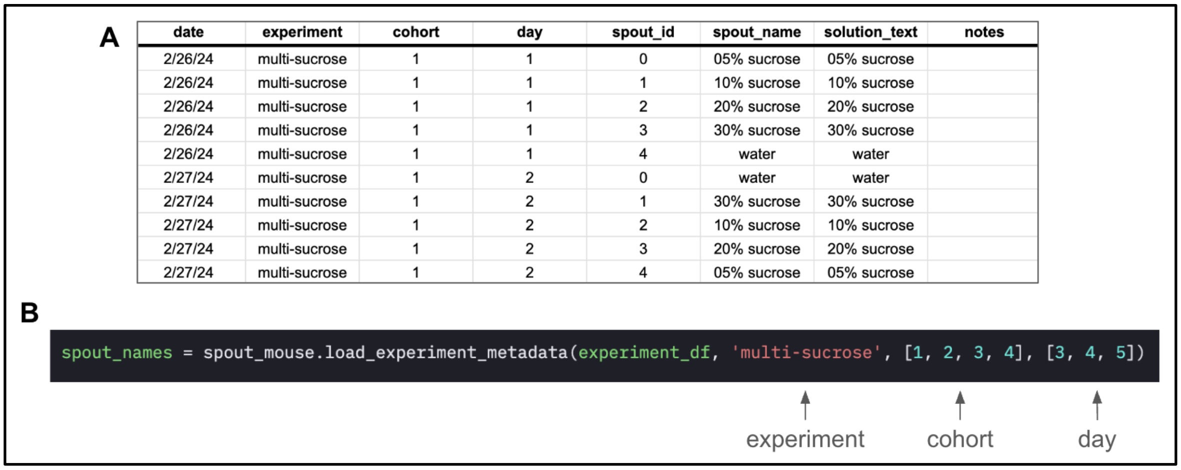

date	experiment	cohort	day	spout_id	spout_name	solution_text	notes
2/26/24	multi-sucrose	1	1	0	05% sucrose	05% sucrose	
2/26/24	multi-sucrose	1	1	1	10% sucrose	10% sucrose	
2/26/24	multi-sucrose	1	1	2	20% sucrose	20% sucrose	
2/26/24	multi-sucrose	1	1	3	30% sucrose	30% sucrose	
2/26/24	multi-sucrose	1	1	4	water	water	
2/27/24	multi-sucrose	1	2	0	water	water	
2/27/24	multi-sucrose	1	2	1	30% sucrose	30% sucrose	
2/27/24	multi-sucrose	1	2	2	10% sucrose	10% sucrose	
2/27/24	multi-sucrose	1	2	3	20% sucrose	20% sucrose	
2/27/24	multi-sucrose	1	2	4	05% sucrose	05% sucrose	

```
spout_names = spout_mouse.load_experiment_metadata(experiment_df, 'multi-sucrose', [1, 2, 3, 4], [3, 4, 5])
```

Figure 10. Google Sheets integration with the Spout Mouse code. (A) Experimental metadata is stored in a Google sheet. (B) To grab all of the spout identities for one experiment, the user runs one line of code specifying the name of the experiment, cohort(s), and day(s) of the experiment to be analyzed.

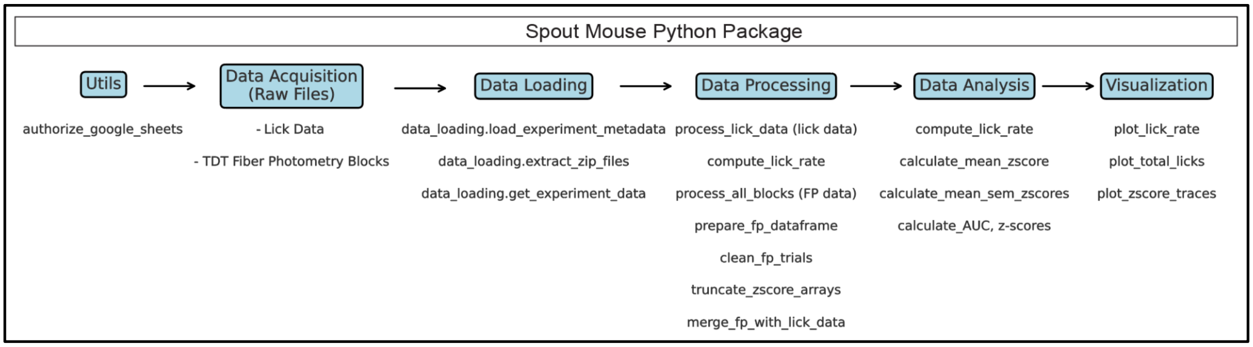

Figure 11. Workflow for Spout Mouse Python Package. Grabs experimental data from Google Sheets, integrates and processes lick data and fiber photometry data, performs simple analysis calculations (e.g. z-score, AUC), and plots data.

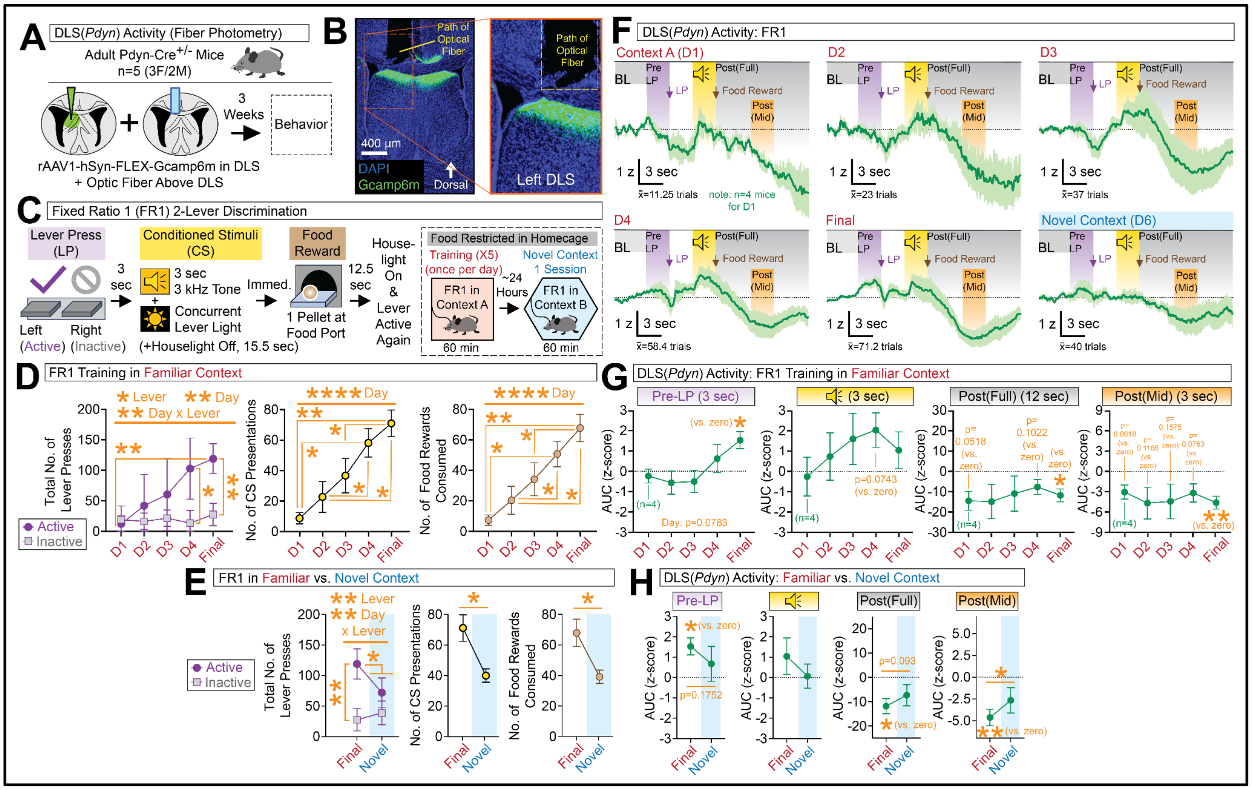

Figure 12. Context-dependent responses of DLS-*Pdyn* neurons during conditioned food reward-seeking (adapted from Goode et al., 2025). (A) *Pdyn*-Cre mice were injected with Cre-dependent GCaMP6m-expressing virus in the dorsal lateral septum (DLS), and an optic fiber was placed above the DLS. (B) Representative coronal image to confirm viral expression and fiber placement. (C) Behavioral design for FR1 2-lever discrimination for a food reward in a familiar vs. novel context. (D) The total number of lever presses, activated CS presentations, and the number of food rewards consumed for each training session. (E) Comparisons of the total number of lever presses, activated CS presentations, and number of food rewards consumed for the final training day vs. in the novel context. (F) Average z- score of the ΔF/F of the GCaMP6m signal aligned to CS onset for all trials from all mice, shown for each session. (G) Area under the curve (AUC) of the z-score of the GCaMP6m signal for specific trial periods during training, including the 3 sec period prior to an active lever press, the 3 sec period during the CS, the 12 sec period following delivery of the

food reward, and the 3 sec period surrounding the midpoint of the post-food reward period. (H) AUC of the z-score of the GCaMP6m signal for specific trial periods during the final day of training vs. in the novel context, including the 3 sec period prior to an active lever press, the 3 sec period during the CS, the 12 sec period following delivery of the food, and the 3 sec period surrounding the midpoint of the post-food reward period. Data are presented as means ±SEM; for all statistics: *$p<0.05$; **$p<0.005$, ***$p<0.0005$; ****$p<0.00005$.

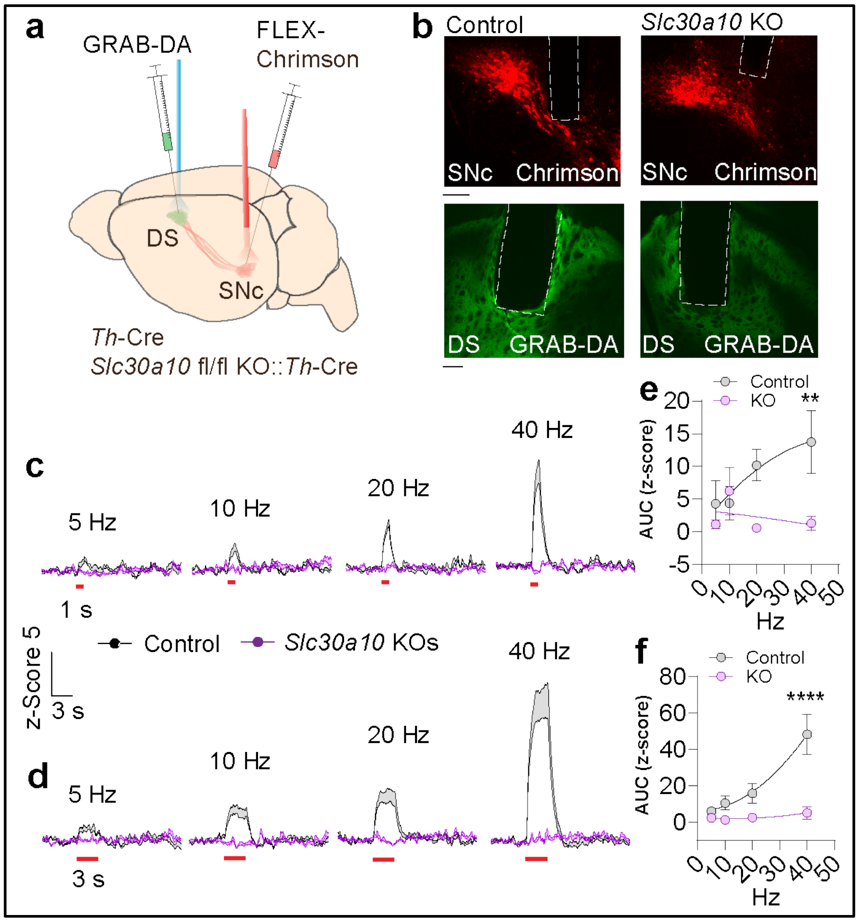

Figure 13. Evoked dopamine release is reduced in *Slc30a10* KO mice (adapted from Grant et al., 2025). (a) Schematic of viral injections and fiber placements for AAV1-GRAB-DA and AAV1-FLEX-Chrimson-tdTomato in *Slc30a10* fl/fl::*Th*-Cre and *Th*-Cre control mice. (b) Example histology for Chrimson expression in the SNc and GRAB-DA expression in the DS of control and KO mice. Dashed lines represent fiber placements. Scale bar = 100 µm. (c-d) GRAB-DA fluorescence following Chrimson stimulation of SNc dopamine neurons for 1s (c) or 3s (d) with increasing stimulation frequency and corresponding AUC calculation (e-f). (N=4 control; N=5 *Slc30a10* fl/fl mice). (e) Two-way repeated measures ANOVA; stimulus x genotype interaction F(3,21)=4.003, P=0.0212; Bonferroni post-hoc, **P=0.0098. (f) Two-way repeated measures ANOVA; stimulus x genotype interaction F(3,21)=12.17, P<0.0001; Bonferroni post-hoc, ****P<0.0001. Data are presented as the mean ± S.E.M.

BIBLIOGRAPHY

1. Abizaid, A., Liu, Z. W., Andrews, Z. B., Shanabrough, M., Borok, E., Elsworth, J. D., Roth, R. H., Sleeman, M. W., Picciotto, M. R., Tschöp, M. H., Gao, X. B., & Horvath, T. L. (2006). Ghrelin modulates the activity and synaptic input organization of midbrain dopamine neurons while promoting appetite. The Journal of clinical investigation, 116(12), 3229–3239. https://doi.org/10.1172/JCI29867.

2. Brogna, S., & Wen, J. (2009). Nonsense-mediated mRNA decay (NMD) mechanisms. Nature structural & molecular biology, 16(2), 107–113. https://doi.org/10.1038/nsmb.1550.

3. Brinkman, E. K., Chen, T., Amendola, M., & van Steensel, B. (2014). Easy quantitative assessment of genome editing by sequence trace decomposition. Nucleic acids research, 42(22), e168. https://doi.org/10.1093/nar/gku936.

4. Catterall W. A. (2011). Voltage-gated calcium channels. Cold Spring Harbor perspectives in biology, 3(8), a003947. https://doi.org/10.1101/cshperspect.a003947.

5. Chen, L. W., Guan, Z. L., & Ding, Y. Q. (1998). Mesencephalic dopaminergic neurons expressing neuromedin K receptor (NK3): a double immunocytochemical study in the rat. Brain research, 780(1), 150–154.

6. Chung, A. S., Miller, S. M., Sun, Y., Xu, X., & Zweifel, L. S. (2017). Sexual congruency in the connectome and translatome of VTA dopamine neurons. Scientific reports, 7(1), 11120. https://doi.org/10.1038/s41598 017-11478-5.

7. Clapham D. E. (2007). Calcium signaling. Cell, 131(6), 1047–1058. https://doi.org/10.1016/j.cell.2007.11.028.

8. Cone, J. J., McCutcheon, J. E., & Roitman, M. F. (2014). Ghrelin acts as an interface between physiological state and phasic dopamine signaling. The Journal of neuroscience: the official journal of the Society for Neuroscience, 34(14), 4905–4913. https://doi.org/10.1523/JNEUROSCI.4404-13.2014.

9. Dacher, M., Gouty, S., Dash, S., Cox, B. M., & Nugent, F. S. (2013). A-kinase anchoring protein-calcineurin signaling in long-term depression of GABAergic synapses. The Journal of neuroscience: the official journal of the Society for Neuroscience, 33(6), 2650–2660. https://doi.org/10.1523/JNEUROSCI.2037-12.2013.

10. El Hamdaoui, Y., Zheng, F., Fritz, N., Ye, L., Tran, M. A., Schwickert, K., Schirmeister, T., Braeuning, A., Lichtenstein, D., Hellmich, U. A., Weikert, D., Heinrich, M., Treccani, G., Schäfer, M. K. E., Nowak, G., Nürnberg, B., Alzheimer, C., Müller, C. P., & Friedland, K. (2022). Analysis of hyperforin (St. John's wort) action at TRPC6 channel leads to the development of a new class of antidepressant drugs. Molecular psychiatry, 27(12), 5070–5085. https://doi.org/10.1038/s41380-022-01804-3.

11. El-Hassar, L., Hagenston, A. M., D'Angelo, L. B., & Yeckel, M. F. (2011). Metabotropic glutamate receptors regulate hippocampal CA1 pyramidal neuron excitability via Ca^{2+} wave-dependent activation of SK and TRPC channels. The Journal of physiology, 589(Pt 13), 3211–3229. https://doi.org/10.1113/jphysiol.2011.209783.

12. Elum, J. E., Szelenyi, E. R., Juarez, B., Murry, A. D., Loginov, G., Zamorano, C. A., Gao, P., Wu, G., Ng-Evans, S., Yee, J. X., Xu, X., Golden, S. A., & Zweifel, L. S. (2024). Distinct dynamics and intrinsic properties in ventral tegmental area populations mediate reward association and motivation. Cell reports, 43(9), 114668. https://doi.org/10.1016/j.celrep.2024.114668.

13. Forman, C. J., Tomes, H., Mbobo, B., Burman, R. J., Jacobs, M., Baden, T., & Raimondo, J. V. (2017). Openspritzer: an open hardware pressure ejection system for reliably delivering picolitre volumes. Scientific reports, 7(1), 2188. https://doi.org/10.1038/s41598-017-02301-2.

14. Gazit Shimoni, N., Tose, A. J., Seng, C., Jin, Y., Lukacsovich, T., Yang, H., Verharen, J. P. H., Liu, C., Tanios, M., Hu, E., Read, J., Tang, L. W., Lim, B. K., Tian, L., Földy, C., & Lammel, S. (2025). Changes in neurotensin signaling drive hedonic devaluation in obesity. Nature, 641(8065), 1238–1247. https://doi.org/10.1038/s41586-025-08748-y.

15. Goode, T. D., Bernstein, M. X., Alipio, J. B., Besnard, A., Pathak, D., Kritzer-Cheren, M. D., Chung, A., Duan, X., Zweifel, L.S. & Sahay, A. (2025). A dorsal hippocampus-prodynorphinergic dorsolateral septum-to-lateral hypothalamus circuit mediates contextual gating of feeding. *Manuscript in revision at Neuron.*

16. Gordon-Fennell, A., Barbakh, J. M., Utley, M. T., Singh, S., Bazzino, P., Gowrishankar, R., Bruchas, M. R., Roitman, M. F., & Stuber, G. D. (2023). An open-source platform for head-fixed operant and consummatory behavior. eLife, 12, e86183. https://doi.org/10.7554/eLife.86183.

17. Gore, B. B., Soden, M. E., & Zweifel, L. S. (2013). Manipulating gene expression in projection-specific neuronal populations using combinatorial viral approaches. Current protocols in neuroscience, 65(435), 4.35.1–4.35.20. https://doi.org/10.1002/0471142301.ns0435s65.

18. Grant, S.M., Bernstein, M. X., Taylor, C., Jursa, T., Zweifel, L.S., Gonzales, R., Smith, D. R. & Mukhopadhyay, S. (2025). Neuron-specific modulation of SLC30A10 identifies dopaminergic and glutamatergic neurons as targets of manganese-induced motor disease. *Manuscript under review at PNAS.*

19. Grove, J. C. R., Gray, L. A., La Santa Medina, N., Sivakumar, N., Ahn, J. S., Corpuz, T. V., Berke, J. D., Kreitzer, A. C., & Knight, Z. A. (2022). Dopamine subsystems that track internal states. Nature, 608(7922), 374–380. https://doi.org/10.1038/s41586-022-04954-0.

20. Khan, R., Laumet, G., & Leinninger, G. M. (2024). Hungry for relief: Potential for neurotensin to address comorbid obesity and pain. Appetite, 200, 107540.

https://doi.org/10.1016/j.appet.2024.107540.

21. Heymann, G., Jo, Y. S., Reichard, K. L., McFarland, N., Chavkin, C., Palmiter, R. D., Soden, M. E., & Zweifel, L. S. (2020). Synergy of Distinct Dopamine Projection Populations in Behavioral Reinforcement. Neuron, 105(5), 909–920.e5. https://doi.org/10.1016/j.neuron.2019.11.024.

22. Hunker, A. C., & Zweifel, L. S. (2020). Protocol to Design, Clone, and Validate sgRNAs for In Vivo Reverse Genetic Studies. STAR protocols, 1(2), 100070. https://doi.org/10.1016/j.xpro.2020.100070.

23. Hsu, T. M., Bazzino, P., Hurh, S. J., Konanur, V. R., Roitman, J. D., & Roitman, M. F. (2020). Thirst recruits phasic dopamine signaling through subfornical organ neurons. Proceedings of the National Academy of Sciences of the United States of America, 117(48), 30744–30754. https://doi.org/10.1073/pnas.2009233117.

24. Hunker, A. C., Soden, M. E., Krayushkina, D., Heymann, G., Awatramani, R., & Zweifel, L. S. (2020). Conditional Single Vector CRISPR/SaCas9 Viruses for Efficient Mutagenesis in the Adult Mouse Nervous System. Cell reports, 30(12), 4303–4316.e6. https://doi.org/10.1016/j.celrep.2020.02.092.

25. Hunker, A. C., & Zweifel, L. S. (2020). Protocol to Design, Clone, and Validate sgRNAs for In Vivo Reverse Genetic Studies. STAR protocols, 1(2), 100070. https://doi.org/10.1016/j.xpro.2020.100070.

26. Kaczmarek, L. K. (1987). The role of protein kinase C in the regulation of ion channels and neurotransmitter release. Trends in Neurosciences 10, 30-34.

27. Kamato, D., Thach, L., Bernard, R., Chan, V., Zheng, W., Kaur, H., Brimble, M., Osman, N., & Little, P. J. (2015). Structure, Function, Pharmacology, and Therapeutic Potential of the G Protein, Gα/q,11. Frontiers in cardiovascular medicine, 2, 14. https://doi.org/10.3389/fcvm.2015.00014.

28. Kelly, M. J., Qiu, J., & Rønnekleiv, O. K. (2018). TRPCing around the hypothalamus. Frontiers in neuroendocrinology, 51, 116–124. https://doi.org/10.1016/j.yfrne.2018.05.004.

29. Kelly, M. J., & Wagner, E. J. (2024). Canonical transient receptor potential channels and hypothalamic control of homeostatic functions. Journal of neuroendocrinology, 36(10), e13392. https://doi.org/10.1111/jne.13392.

30. Khan, R., Laumet, G., & Leinninger, G. M. (2024). Hungry for relief: Potential for neurotensin to address comorbid obesity and pain. *Appetite*, *200*, 107540. https://doi.org/10.1016/j.appet.2024.107540.

31. Klipec, W. D., Burrow, K. R., O'Neill, C., Cao, J. L., Lawyer, C. R., Ostertag, E., Fowler, M., Bachtell, R. K., Illig, K. R., & Cooper, D. C. (2016). Loss of the trpc4 gene is associated with

a reduction in cocaine self-administration and reduced spontaneous ventral tegmental area dopamine neuronal activity, without deficits in learning for natural rewards. Behavioural brain research, 306, 117–127. https://doi.org/10.1016/j.bbr.2016.03.027.

32. Lein, E. S., Hawrylycz, M. J., Ao, N., Ayres, M., Bensinger, A., Bernard, A., Boe, A. F., Boguski, M. S., Brockway, K. S., Byrnes, E. J., Chen, L., Chen, L., Chen, T. M., Chin, M. C., Chong, J., Crook, B. E., Czaplinska, A., Dang, C. N., Datta, S., Dee, N. R., … Jones, A. R. (2007). Genome-wide atlas of gene expression in the adult mouse brain. Nature, 445(7124), 168–176. https://doi.org/10.1038/nature05453.

33. Liu, Y., Harding, M., Pittman, A., Dore, J., Striessnig, J., Rajadhyaksha, A., & Chen, X. (2014). Cav1.2 and Cav1.3 L-type calcium channels regulate dopaminergic firing activity in the mouse ventral tegmental area. Journal of neurophysiology, 112(5), 1119–1130. https://doi.org/10.1152/jn.00757.2013.

34. Luo, Y., Sun, L., & Peng, Y. (2025). The structural basis of the G protein-coupled receptor and ion channel axis. Current research in structural biology, 9, 100165. https://doi.org/10.1016/j.crstbi.2025.100165.

35. Mathes, C., & Thompson, S. H. (1994). Calcium current activated by muscarinic receptors and thapsigargin in neuronal cells. *The Journal of general physiology*, *104*(1), 107–121. https://doi.org/10.1085/jgp.104.1.107.

36. Merrill, C. B., Friend, L. N., Newton, S. T., Hopkins, Z. H., & Edwards, J. G. (2015). Ventral tegmental area dopamine and GABA neurons: Physiological properties and expression of mRNA for endocannabinoid biosynthetic elements. Scientific reports, 5, 16176. https://doi.org/10.1038/srep16176.

37. Meye, F. J., & Adan, R. A. (2014). Feelings about food: the ventral tegmental area in food reward and emotional eating. Trends in pharmacological sciences, 35(1), 31–40. https://doi.org/10.1016/j.tips.2013.11.003.

38. Mietlicki-Baase, E. G., Santollo, J., & Daniels, D. (2021). Fluid intake, what's dopamine got to do with it?. Physiology & behavior, 236, 113418. https://doi.org/10.1016/j.physbeh.2021.113418.

39. Naef, L., Pitman, K. A., & Borgland, S. L. (2015). Mesolimbic dopamine and its neuromodulators in obesity and binge eating. CNS spectrums, 20(6), 574–583. https://doi.org/10.1017/S1092852915000693.

40. Nalivaiko, E., Michaud, J. C., Soubrié, P., Le Fur, G., & Feltz, P. (1997). Tachykinin neurokinin-1 and neurokinin-3 receptor-mediated responses in guinea-pig substantia nigra: an in vitro electrophysiological study. *Neuroscience*, *78*(3), 745–757. https://doi.org/10.1016/s0306-4522(96)00625-2.

41. Ningoo, M., Plant, L. D., Greka, A., & Logothetis, D. E. (2021). PIP2 regulation of TRPC5 channel activation and desensitization. The Journal of biological chemistry, 296, 100726. https://doi.org/10.1016/j.jbc.2021.100726.

42. Palacios-Muñoz, A., de Paula Moreira, D., Silva, V., García, I. E., Aboitiz, F., Zarrei, M., Campos, G., Rennie, O., Howe, J. L., Anagnostou, E., Ambrozewic, P., Scherer, S. W., Passos-Bueno, M. R., & Ewer, J. (2022). Mutations in trpγ, the homologue of TRPC6 autism candidate gene, causes autism-like behavioral deficits in Drosophila. Molecular psychiatry, 27(8), 3328–3342. https://doi.org/10.1038/s41380-022-01555-1.

43. Palmiter R. D. (2007). Is dopamine a physiologically relevant mediator of feeding behavior?. Trends in neurosciences, 30(8), 375–381. https://doi.org/10.1016/j.tins.2007.06.004.

44. Parker, J. G., Wanat, M. J., Soden, M. E., Ahmad, K., Zweifel, L. S., Bamford, N. S., & Palmiter, R. D. (2011). Attenuating GABA(A) receptor signaling in dopamine neurons selectively enhances reward learning and alters risk preference in mice. The Journal of neuroscience: the official journal of the Society for Neuroscience, 31(47), 17103–17112. https://doi.org/10.1523/JNEUROSCI.1715-11.2011.

45. Perez-Bonilla, P., Santiago-Colon, K., & Leinninger, G. M. (2020). Lateral hypothalamic area neuropeptides modulate ventral tegmental area dopamine neurons and feeding. Physiology & behavior, 223, 112986. https://doi.org/10.1016/j.physbeh.2020.112986.

46. Qiu, J., Nestor, C. C., Zhang, C., Padilla, S. L., Palmiter, R. D., Kelly, M. J., & Rønnekleiv, O. K. (2016). High-frequency stimulation-induced peptide release synchronizes arcuate kisspeptin neurons and excites GnRH neurons. eLife, 5, e16246. https://doi.org/10.7554/eLife.16246.

47. Qiu, J., Stincic, T. L., Bosch, M. A., Connors, A. M., Kaech Petrie, S., Rønnekleiv, O. K., & Kelly, M. J. (2021). Deletion of Stim1 in Hypothalamic Arcuate Nucleus Kiss1 Neurons Potentiates Synchronous GCaMP Activity and Protects against Diet-Induced Obesity. The Journal of neuroscience: the official journal of the Society for Neuroscience, 41(47), 9688–9701. https://doi.org/10.1523/JNEUROSCI.0622-21.2021.

48. Qiu, J., Voliotis, M., Bosch, M. A., Li, X. F., Zweifel, L. S., Tsaneva-Atanasova, K., O'Byrne, K. T., Rønnekleiv, O. K., & Kelly, M. J. (2024). Estradiol elicits distinct firing patterns in arcuate nucleus kisspeptin neurons of females through altering ion channel conductances eLife 13:RP96691. https://doi.org/10.7554/eLife.96691.4.

49. Ramirez-Virella, J., & Leinninger, G. M. (2021). The Role of Central Neurotensin in Regulating Feeding and Body Weight. Endocrinology, 162(5), bqab038. https://doi.org/10.1210/endocr/bqab038.

50. Razidlo, J. A., Fausner, S. M. L., Ingebretson, A. E., Wang, L. C., Petersen, C. L., Mirza, S., Swank, I. N., Alvarez, V. A., & Lemos, J. C. (2022). Chronic Loss of Muscarinic M5 Receptor Function Manifests Disparate Impairments in Exploratory Behavior in Male and Female Mice

despite Common Dopamine Regulation. The Journal of neuroscience: the official journal of the Society for Neuroscience, 42(36), 6917–6930. https://doi.org/10.1523/JNEUROSCI.1424-21.2022.

51. Sato, H., & Singer, R. H. (2021). Cellular variability of nonsense-mediated mRNA decay. Nature communications, 12(1), 7203. https://doi.org/10.1038/s41467-021-27423-0.

52. Schultz, W., Dayan, P., & Montague, P. R. (1997). A neural substrate of prediction and reward. Science (New York, N.Y.), 275(5306), 1593–1599. https://doi.org/10.1126/science.275.5306.1593.

53. Seutin, V., Massotte, L., & Dresse, A. (1989). Electrophysiological effects of neurotensin on dopaminergic neurones of the ventral tegmental area of the rat in vitro. *Neuropharmacology*, *28*(9), 949–954. https://doi.org/10.1016/0028-3908(89)90194-9.

54. Shead, N. W., & Hodgins, D. C. (2009). Probability discounting of gains and losses: implications for risk attitudes and impulsivity. Journal of the experimental analysis of behavior, 92(1), 1–16. https://doi.org/10.1901/jeab.2009.92-1.

55. Shin, K. C., Ali, G., Ali Moussa, H. Y., Gupta, V., de la Fuente, A., Kim, H. G., Stanton, L. W., & Park, Y. (2023). Deletion of TRPC6, an Autism Risk Gene, Induces Hyperexcitability in Cortical Neurons Derived from Human Pluripotent Stem Cells. Molecular neurobiology, 60(12), 7297–7308. https://doi.org/10.1007/s12035-023-03527-0.

56. Simms, B. A., & Zamponi, G. W. (2014). Neuronal voltage-gated calcium channels: structure, function, and dysfunction. Neuron, 82(1), 24–45. https://doi.org/10.1016/j.neuron.2014.03.016.

57. Simon, R. C., Loveless, M. C., Yee, J. X., Goh, B., Cho, S. G., Nasir, Z., Hashikawa, K., Stuber, G. D., Zweifel, L. S., & Soden, M. E. (2024). Opto-seq reveals input-specific immediate-early gene induction in ventral tegmental area cell types. Neuron, 112(16), 2721–2731.e5. https://doi.org/10.1016/j.neuron.2024.05.026.

58. Simpson, E. H., Akam, T., Patriarchi, T., Blanco-Pozo, M., Burgeno, L. M., Mohebi, A., Cragg, S. J., & Walton, M. E. (2024). Lights, fiber, action! A primer on in vivo fiber photometry. *Neuron*, *112*(5), 718–739. https://doi.org/10.1016/j.neuron.2023.11.016.

59. Soden, M. E., Yee, J. X., Cuevas, B., Rastani, A., Elum, J., & Zweifel, L. S. (2022). Distinct Encoding of Reward and Aversion by Peptidergic BNST Inputs to the VTA. Frontiers in neural circuits, 16, 918839. https://doi.org/10.3389/fncir.2022.918839.

60. Soden, M. E., Yee, J. X., & Zweifel, L. S. (2023). Circuit coordination of opposing neuropeptide and neurotransmitter signals. Nature, 619(7969), 332–337. https://doi.org/10.1038/s41586-023-06246-7.

61. Sonkusare, S. K., Dalsgaard, T., Bonev, A. D., Hill-Eubanks, D. C., Kotlikoff, M. I., Scott, J. D., Santana, L. F., & Nelson, M. T. (2014). AKAP150-dependent cooperative TRPV4 channel gating is central to endothelium-dependent vasodilation and is disrupted in hypertension. Science signaling, 7(333), ra66. https://doi.org/10.1126/scisignal.2005052.

62. Stuhrman, K., & Roseberry, A. G. (2015). Neurotensin inhibits both dopamine- and GABA-mediated inhibition of ventral tegmental area dopamine neurons. Journal of neurophysiology, 114(3), 1734–1745. https://doi.org/10.1152/jn.00279.2015.

63. Suh, B. C., & Hille, B. (2002). Recovery from muscarinic modulation of M current channels requires phosphatidylinositol 4,5-bisphosphate synthesis. *Neuron*, *35*(3), 507–520. https://doi.org/10.1016/s0896-6273(02)00790-0.

64. Ting, J. T., Daigle, T. L., Chen, Q., & Feng, G. (2014). Acute brain slice methods for adult and aging animals: application of targeted patch clamp analysis and optogenetics. Methods in molecular biology (Clifton, N.J.), 1183, 221–242. https://doi.org/10.1007/978-1-4939-1096-0_14.

65. Torruella-Suárez, M. L., & McElligott, Z. A. (2020). Neurotensin in reward processes. Neuropharmacology, 167, 108005. https://doi.org/10.1016/j.neuropharm.2020.108005.

66. Tracy, M. E., Tesic, V., Stamenic, T. T., Joksimovic, S. M., Busquet, N., Jevtovic-Todorovic, V., & Todorovic, S. M. (2018). CaV3.1 isoform of T-type calcium channels supports excitability of rat and mouse ventral tegmental area neurons. Neuropharmacology, 135, 343–354. https://doi.org/10.1016/j.neuropharm.2018.03.028.

67. Wang, H., Cheng, X., Tian, J., Xiao, Y., Tian, T., Xu, F., Hong, X., & Zhu, M. X. (2020). TRPC channels: Structure, function, regulation and recent advances in small molecular probes. Pharmacology & therapeutics, 209, 107497. https://doi.org/10.1016/j.pharmthera.2020.107497.

68. Wang, J., Su, M., Zhang, D., Zhang, L., Niu, C., Li, C., You, S., Sang, Y., Zhang, Y., Du, X., & Zhang, H. (2024). The cation channel mechanisms of subthreshold inward depolarizing currents in the mice VTA dopaminergic neurons and their roles in the chronic-stress-induced depression-like behavior. eLife, 12, RP88319. https://doi.org/10.7554/eLife.88319.

69. Wang, Q., Wang, D., Shibata, S., Ji, T., Zhang, L., Zhang, R., Yang, H., Ma, L., & Jiao, J. (2019). Group I metabotropic glutamate receptor activation induces TRPC6-dependent calcium influx and RhoA activation in cultured human kidney podocytes. *Biochemical and biophysical research communications*, *511*(2), 374–380. https://doi.org/10.1016/j.bbrc.2019.02.062.

70. Wise R. A. (2004). Dopamine, learning and motivation. Nature reviews. Neuroscience, 5(6), 483–494. https://doi.org/10.1038/nrn1406.

71. Won, J., Kim, J., Jeong, H., Kim, J., Feng, S., Jeong, B., Kwak, M., Ko, J., Im, W., So, I., & Lee, H. H. (2023). Molecular architecture of the Gαi-bound TRPC5 ion channel. Nature communications, 14(1), 2550. https://doi.org/10.1038/s41467-023-38281-3.

72. Wong, W., & Scott, J. D. (2004). AKAP signaling complexes: focal points in space and time. Nature reviews. Molecular cell biology, 5(12), 959–970. https://doi.org/10.1038/nrm1527.

73. Wu, L., Bauer, C. S., Zhen, X. G., Xie, C., & Yang, J. (2002). Dual regulation of voltage-gated calcium channels by PtdIns(4,5)P2. Nature, 419(6910), 947–952. https://doi.org/10.1038/nature01118.

74. Yeomans, J., Forster, G., & Blaha, C. (2001). M5 muscarinic receptors are needed for slow activation of dopamine neurons and for rewarding brain stimulation. *Life sciences*, *68*(22-23), 2449–2456. https://doi.org/10.1016/s0024-3205(01)01038-4.

75. Yeon, J., Kim, J., Kim, D. Y., Kim, H., Kim, J., Du, E. J., Kang, K., Lim, H. H., Moon, D., & Kim, K. (2018). A sensory-motor neuron type mediates proprioceptive coordination of steering in C. elegans via two TRPC channels. PLoS biology, 16(6), e2004929. https://doi.org/10.1371/journal.pbio.2004929

76. Zaydman, M. A., & Cui, J. (2014). PIP2 regulation of KCNQ channels: biophysical and molecular mechanisms for lipid modulation of voltage-dependent gating. Frontiers in physiology, 5, 195. https://doi.org/10.3389/fphys.2014.00195.

77. Zernov, N., & Popugaeva, E. (2023). Role of Neuronal TRPC6 Channels in Synapse Development, Memory Formation and Animal Behavior. International journal of molecular sciences, 24(20), 15415. https://doi.org/10.3390/ijms242015415.

78. Zhang, L., Guo, F., Kim, J. Y., & Saffen, D. (2006). Muscarinic acetylcholine receptors activate TRPC6 channels in PC12D cells via Ca2+ store-independent mechanisms. *Journal of biochemistry*, *139*(3), 459–470. https://doi.org/10.1093/jb/mvj065.

79. Zhang, M., Ma, Y., Ye, X., Zhang, N., Pan, L., & Wang, B. (2023). TRP (transient receptor potential) ion channel family: structures, biological functions and therapeutic interventions for diseases. Signal transduction and targeted therapy, 8(1), 261. https://doi.org/10.1038/s41392-023-01464-x.

80. Zhang, W. W., Wang, Y., & Chu, Y. X. (2020). Tacr3/NK3R: Beyond Their Roles in Reproduction. ACS chemical neuroscience, 11(19), 2935–2943. https://doi.org/10.1021/acschemneuro.0c00421.

81. Zweifel, L. S., Parker, J. G., Lobb, C. J., Rainwater, A., Wall, V. Z., Fadok, J. P., Darvas, M., Kim, M. J., Mizumori, S. J., Paladini, C. A., Phillips, P. E., & Palmiter, R. D. (2009). Disruption of NMDAR-dependent burst firing by dopamine neurons provides selective assessment of phasic dopamine-dependent behavior. Proceedings of the National Academy of

Sciences of the United States of America, 106(18), 7281 7288. https://doi.org/10.1073/pnas.0813415106.